Chemical Engineering Science 318 (2025) 122166

Contents lists available at ScienceDirect

Chemical Engineering Science

journal homepage: www.elsevier.com/locate/ces

Steady and dynamic state simulation of a methanol continuous-flow laboratory reactor for process variable evaluation and event-based thermostat regulation

Samuel Emebu [a,*], Esko Juhani Lahdenpera [a], Michael Chukwuemeka Ekwonu [c], Ibrahim Shaikh [b], Arto Laari [a], Ojeaga Imanah [d], Nima Rezaei [a], Kim Dong [c], Tuomas Koiranen [a]

[a] Department of Separation Science, Lappeenranta-Lahti University of Technology LUT, Yliopistonkatu 34, FI-53850 Lappeenranta, Finland
[b] Department of Automation and Control Engineering, Faculty of Applied Informatics, Tomas Bata University in Zlín, Nad Stráněmi 4511, 760 05 Zlín, Czech Republic
[c] School of Mechanical Engineering, University of Ulsan, Republic of Korea
[d] Department of Chemistry, University of Benin, Nigeria

ARTICLE INFO

Keywords:
Methanol synthesis
Power-to-x
Dynamic model
Steady-state model
COMSOL
Thermostat

ABSTRACT

Power-to-X (P2X) converts excess renewable energy into hydrogen and then renewable fuels like methanol, addressing hydrogen storage costs. Methanol synthesis uses catalysts such as Cu/ZnO/Al2O3, with performance influenced by pressure, hydrogen-to-carbon ratio, and temperature. Therefore, accurate modelling, using kinetics like Graaf et al. Langmuir-Hinshelwood-Hougen-Watson type model, material, momentum, and energy balances within the reactor, is essential. Based on these models, the performance of methanol synthesis was analysed. Specifically, analysis of bed porosity ($\varepsilon_{pm} = 0.1 - 0.5$), stoichiometric ratio of hydrogen-to-carbon (SH = 1 – 3), Gas-Hourly-Space-Velocity (GHSV = 1400 – 8400 h^{-1}), temperature (200 – 280 °C) and pressure (20 – 60 bar) on the methanol synthesis performance for both dynamic and steady-state conditions was performed via COMSOL Multiphysics. This was followed by a thermostatic regulation of the reaction temperature between 239 – 241 °C, model application to simulate an in-house laboratory digital twin Micromeritics reactor, in addition to an industrial-sized reactor.

1. Introduction

According to the International Energy Agency (IEA)'s 2023 report on renewable energy, the world's renewable energy capacity has been rapidly expanding over the last three decades. Based on this trend, a forecast has been made that aims to triple global capacity by 2030, as set by governments in the COP28 UN Climate Change Conference (International Energy Agency (IEA). Massive expansion of renewable power opens door to achieving global tripling goal set at COP28, 2024). Specifically, the amount of renewable energy capacity added to the global energy system increased by 50 %, reaching about 510 GW (GW) in 2023, with solar photovoltaics accounting for three-quarters of this increase (International Energy Agency (IEA). Massive expansion of renewable power opens door to achieving global tripling goal set at COP28, 2024). Over the next five years (i.e., by 2028), it is proposed that solar photovoltaics and wind energy will account for 96 % of this renewable energy expansion. This is because their generation cost is lower than that of other energy sources, and they are currently favoured by the energy policies of most countries (International Energy Agency (IEA). Solar PV, 2023). The rise in solar photovoltaics and wind energy, as already being observed, can exacerbate the issue of excess or surplus energy generation, i.e., unused energy. Typically, this situation arises when backup batteries are fully charged or when the minimum energy generated exceeds the available energy demand. Thus, the excess energy must either be dumped or curtailed (Vaziri Rad et al., 2023; O'Shaughnessy et al., 2020). In mitigating solar or wind energy curtailment, a long-term viable solution is to convert excess generated energy into fuels. The produced fuel can then be used for stationary energy production or transportation, thus overcoming the limitations of electrical energy storage. This energy-to-fuel transition is termed power-to-x (P2X) (Ince et al., 2021), with power-to-hydrogen (PtH) forming the basis for many P2X pathways. Hydrogen gas can be easily produced from renewable energy through water electrolysis. Hydrogen is considered a

* Corresponding author.
E-mail address: samuel.emebu@lut.fi (S. Emebu).

https://doi.org/10.1016/j.ces.2025.122166
Received 26 September 2024; Received in revised form 19 May 2025; Accepted 2 July 2025
Available online 4 July 2025

Nomenclature

List of abbreviations

Abbreviations	Meaning and unit
GHSV	Gas-Hourly-Space-Velocity, (h^{-1})
LHHW	Langmuir-Hinshelwood-Hougen-Watson
SH	Stoichiometric ratio of hydrogen to carbon (−)
TC	Temperature sensors and controller
PC	Pressure regulator
PDEs	Partial differential equations
FEM	Finite element method
RWGS	Reverse water gas shift

List of symbols

Symbols	Meaning and unit
r_p	Catalyst radius and diameter, d_p=2 r_p (μm)
D_{R-i} and D_{R-o}	Inner and outer diameter of reactor, (mm)
$\overline{D}_R$	Reactor logarithmic diameter, $\overline{D}_R = (D_{R-i} - D_{R-i})/\ln(D_{R-o}/D_{R-i})$ (mm)
x_w	Reactor thickness, $x_w = 0.5(D_{R-o} - D_{R-i})$, (mm)
D_C	Hydraulic diameter of cooling jacket, (mm)
L	Total length of parent tube, (mm)
L_{pm}	Length of catalyst bed/matrix, (mm)
L_{R-i} and L_{R-o}	Length of reactor inlet and outlet section, L_{R-i} = L_{R-o}= 0.5(L – L_{pm}), (mm)
A_{R-i}	Inner wall surface area of reactor/catalyst bed, A_{R-i}= $\pi D_{R-i} L_{pm}$, (m^2)
A_{R-o}	Cooling tube surface area, A_{R-o}= $\pi D_C L_{pm}$, (m^2)
$\overline{A}_w$	Logarithmic area, $\overline{A}_w$= $\pi \overline{D}_R L_{pm}$, ($m^2$)
$V_{\nearrow}$	Volume of catalyst bed,$V_{\nearrow} = \pi(D^2_{R-i}/4)L_{pm}$, ($m^3$)
V_c	volume of cooling tube, V_c= $\pi(D_C^2/4)L_{pm}$
y_{j_*} or y_j	Molar fractions of reactor species
C_j and C_{o-j}	Molar and initial concentration of species j, (mol m^{-3})
R_j	Reactive terms considered, R_j= $\alpha \Sigma n_j r_{\nearrow} \rho_p$, (mol m^{-3} s^{-1})
α and α_o	Catalyst and initial catalyst activity, (−)
n_j	Reactive molar stoichiometric for each species (−)
$r_{\nearrow}$	Rate-based kinetic models,$_{\nearrow}$ = 1, 2&3, (mol kg_{ct}^{-1} s^{-1})
ρ, ρ_c and ρ_p	Reactor fluid, coolant fluid, and catalyst density, (kg m^{-3})
u or **u**	Fluid velocity field or Darcy velocity, (m s^{-1})
D_{eff-j}	Effective diffusivity, $D_{eff-j} = \varepsilon_{pm} D_{m-j}/\tau_{pm}$ (m^2 s^{-1})
D_{m-j}	Species diffusivity through the mixture, (m^2 s^{-1})
D_{jj_*}	The diffusivity of binary gases, (m^2 s^{-1})
τ_{pm}	Matrix tortuosity, $\tau_{pm} = \varepsilon_{pm}^{-1/3}$(−)
ε_{pm}	Bed porosity or porosity of catalyst matrix (−)
ε_p	Catalyst porosity, (−)
n	Vector direction outward (−)
ΔP	Pressure drops across the porous matrix.
μ, and μ_c	Reacting fluid and coolant fluid dynamic viscosity, (kg m^{-1} s^{-1})
μ_{c*} and μ_{wc}	Coolant viscosity at bulk, T_c and cold wall temperature, T_{wc}, (kg m^{-1} s^{-1})
κ	Matrix permeability, $\kappa = d_p^2 \varepsilon_{pm}^3/180(1-\varepsilon_{pm})^2$, ($m^2$)
β	Non-darcy flow coefficient, $\beta = 1.75(1-\varepsilon_{pm})/d_p \varepsilon_{pm}^3$, ($m^{-1}$)
g	Gravity, (m s^{-2})
F	Forchheimer and Ergun drag viscous force, F = $-\beta\rho|u|u$, (kg m^{-2} s^{-2})
P_j	Partial pressure for reacting species, j (bar)
P_o	Initial/reaction pressure, P_o, (bar)
θ_*	Catalyst adsorption coverage term ($bar^{-0.5}$)
K_1, K_2, and K_3	K_1, K_2 (bar^{-1}) are adsorption constants for CO, CO_2, and K_3 ($bar^{-0.5}$) is a modified form of adsorption constants to account for the interactive effect of H_2 and H_2O
K_{E1}, K_{E2}, K_{E3}	K_{E1}, K_{E2} (bar^{-2}) are modified equilibrium constants for $r_{MEOH-CO}$, $r_{MEOH-CO_2}$, and K_{E3}(−) is equilibrium constant for r_{RWGS}
K_{P1}, K_{P2}, K_{P3}	K_{P1}, K_{P2}(mol kg_{ct}^{-1} s^{-1} bar^{-1}) are reaction constant for $r_{MEOH-CO}$, $r_{MEOH-CO_2}$, and K_{P3} (mol kg_{ct}^{-1} s^{-1} $bar^{-0.5}$) for r_{RWGS}
k	Viscous stress tensor, **k** = $\mu/\varepsilon_{pm}\left(\nabla u + (\nabla u)^T\right) - 2\mu/3\varepsilon_{pm}(\nabla u)I$, (Pa)
I	Signifies identity matrix
$(\rho C_P)_{eff}$	Effective volumetric heat capacity, $(\rho C_P)_{eff} = \epsilon_{pm}\rho C_P + (1-\epsilon_{pm})\rho_p C_{Pp}$(J m^{-3} K^{-1})
C_P, C_{Pc} and C_{Pp}	Reacting fluid, coolant fluid, and catalyst heat capacity, (J kg^{-1} K^{-1})
k_{eff}	Effective thermal conductivity, $k_{eff} = \epsilon_{pm}k + (1-\epsilon_{pm})k_p$, (W m^{-1} K^{-1})
k and k_p	Fluid and catalyst thermal conductivity, (W m^{-1} K^{-1})
k_c and k_w	Coolant and reactor wall thermal conductivity, (W m^{-1} K^{-1})
$\Delta H_{\nearrow}$	Heat of reaction, (J mol^{-1})
T	Reactor temperature, (K)
T_{wh}	Reactor hot/inside wall temperature, (K)
T_{wc}	Cold/outer wall temperature, (K)
T_c	Coolant temperature, (K)
T_f	Reactor film temperature, T_f = 0.5(T_{wh} + T), (K)
T_{fc}	Coolant film temperature, T_{fc} = 0.5(T_{wc} + T_c), (K)
T_o and T_{oc}	Initial/isothermal reactor and coolant temperature, (K)
h_R	Reactor heat coefficient, (W m^{-2} K^{-1})
h_C	Coolant heat coefficient, (W m^{-2} K^{-1})
U_i	Overall heat coefficient, (W m^{-2} K^{-1})
Q_{R-W}	Heat transfer from reactor to its wall, Q_{R-W}= $A_{R-i}h_R(T - T_{wh})$, (W)
Q_{W-C}	Heat transfer from reactor outer wall surface to coolant, Q_{W-C}= $A_{R-o}h_C(T_{wc} - T_c)$, (W)
Q_{R-C}	Heat transfer from reactor content to coolant, Q_{R-C}= $U_i A_{R-i}(T - T_c)$ (W)
Q_W	Heat transfer from reactor cold wall surface, Q_W = $\overline{A}_w(k_w/x_w)(T_{wh} - T_{wc})$, (W)
Q_C	Cooling supplied, Q_C= $q_c\rho_c C_{Pc}(T_c - T_{oc})$, (W)
q_c	Volumetric flowrate of coolant, (m^3 s^{-1})
Re and Re_c	Reynold no. for reacting, Re = $\rho u D_{R-i}/\mu$, and coolant fluids, Re_c = $\rho_c u_c D_C/\mu_c$, (−)
Nu_R and Nu_C	Nusselt no. for reacting, Nu_R=$h_R D_{R-i}/k$ and coolant fluids, Nu_C=$h_C D_c/k_c$ (−)
Pr and Pr_c	Prandtl number for reacting, Pr = $C_P\mu/k$, and coolant fluids, Pr_c = $C_{Pc}\mu_c/k_c$ (−)
E_d	Catalyst deactivation energy, (J mol^{-1})
T_d	Catalyst deactivation reference temperature, (K)
K_d	Catalyst deactivation constant, (h^{-1})
R	R is idea1 gas constant, 8.3145 (J mol^{-1} K^{-1})*COMSOL automatically harmonizes all units into SI units

List of Subscript, and superscript

Subscript, & superscript	Meaning and unit
R	Subscript "R" denotes reactor
i	Subscript "i" denotes inlet
o	Subscript "o" denotes initial or sometimes outlet
w	Subscript "w" denotes wall, properties
c	Subscript, "c" denotes coolant
j or j_*	Subscript for reactive molar stoichiometric for each species,j = CO, CO_2, H_2, N_2, CH_3OH, H_2O
$_{\nearrow}$	Subscript$_{\nearrow}$ = 1 = MEOH−CO, 2 = MEOH−CO2, and 3 = RWGS
T	Superscript implies transpose

promising energy carrier due to its high gravimetric energy density, Table 1 (Palys and Daoutidis, 2022). However, challenges such as high storage costs associated with its pressurization, and its lower volumetric energy density, compared to its derivatives like methanol, ethanol, and ammonia, have encouraged its subsequent conversion into other renewable fuels. These derivatives offer improved storage and utilisation characteristics (Palys and Daoutidis, 2022).

Among these derivatives, power-to-methanol (PtM) is a promising approach. It involves combining hydrogen produced via power-to-hydrogen (PtH) with carbon sources (carbon monoxide and dioxide) captured from industrial or biogenic emissions, Equation (1) – (3) (Graaf et al., 1988; Nestler et al., 2020). This pathway not only facilitates efficient storage and transport of renewable energy in liquid form but also supports carbon recycling, thereby contributing to climate change mitigation.

$$CO + 2H_2 \leftrightarrow CH_3OH\ \Delta H^{298K} = -90.77\ KJ.mol^{-1} \quad (1)$$

$$CO_2 + 3H_2 \leftrightarrow CH_3OH + H_2O\ \Delta H^{298K} = -49.16\ KJ.mol^{-1} \quad (2)$$

$$CO_2 + H_2 \leftrightarrow CO + H_2O\ \Delta H^{298K} = +41.21\ KJ.mol^{-1} \quad (3)$$

$$SH = n_{H_2}/(2n_{CO} + 3n_{CO_2}) \geq 1.0 \quad (4)$$

Methanol production via the PtM framework is achieved by the hydrogenation of carbon monoxide (CO) and/or carbon dioxide (CO_2) in the presence of suitable heterogeneous catalysts, such as $Cu/ZnO/Al_2O_3$, $Pd/ZnO/Al_2O_3$, $GaPd_2/SiO_2$, In_2O_3/ZrO_2, and others (Stangeland et al., 2020), typically within a packed bed reactor. The reaction generally requires a minimum temperature of 200 °C, 35 to 148 atm pressure, and a hydrogen (n_{H_2}) to carbon (n_{CO} and n_{CO_2}) mole ratio of at least one, Equation (4) (Emebu et al., 2023). The efficiency of methanol production depends on the catalyst type, and its physicochemical characteristics, as well as the combined, and interactive effects of reaction temperature, and pressure (Borisut and Nuchitprasittichai, 2019). This is because, for each specific catalyst, the reaction conditions, especially temperature and pressure are typically optimised to maximise performance (Ledakowicz et al., 2013). Typical methanol yields from CO_2, and CO hydrogenation for various catalysts are highlighted in literature (Nielsen et al., 2020; Dieterich et al., 2020). Therefore, it is necessary to adequately measure reactor's temperature and pressure to maintain optimal operating conditions, ensure product quality, maximise energy efficiency, and minimise pollutant emissions. However, packed bed reactors are typically composed of catalyst particles that exhibit variations in shape, size, surface morphology, density, hardness, pore distribution, adsorption properties, etc (Barbosa-Cánovas et al., 2005). Given that methanol synthesis typically occurs at high temperatures,200 – 320 °C, accurately measuring temperature within the reactor can be challenging. This difficulty arises due to the heterogeneous distribution of fluids in the packed bed, which can lead to uneven temperature profiles or the formation of hot spots in various sections of the reactor (Zhang et al., 2022). These issues can be addressed using advanced techniques such as multi-sensor arrays, and surface field temperature measurements (Xuan et al., 2024; Schäfer et al., 2013). However, these methods are often complex to install (Bahiraei, 2019), and expensive to both implement and maintain (Blay and Bobadilla, 2018), especially in industrial reactors. As a simpler and more cost-effective alternative to direct measurements, numerical modeling can be employed to simulate the temperature dynamics within the reactor. The concept of numerical model development as an alternative to direct measurement involves developing models that comprehensively account for all relevant mass, momentum, and heat transfer phenomena (Kutscherauer et al., 2022) within the reactor. The results of such numerical models can be validated with experimental results from a laboratory-scale or micrometric-scale reactor, where direct measurements are generally easier and cheaper to implement. Using small-scale reactors for validation is essential, as numerical simulations of thermochemical processes in larger packed-bed reactors remain challenging. This complexity arises from the large computational domain, the multi-scale nature of the system, and the presence of various heat transfer modes such as particle-to-particle conduction, and convective, conductive, and radiative heat exchange between the reactor and its surroundings (Xuan et al., 2024).

Numerous studies in literature on the modelling of methanol reactors, under both dynamic and steady-state conditions. These models are typically developed based on specific assumptions regarding reaction kinetics, as well as mass, momentum, and heat transfer phenomena (Leonzio and Foscolo, 2020; Rahimpour et al., 2009; Parvasi et al., 2008; Zhu et al., 2020; Hafeez et al., 2020; Bakhtiary et al., 2024; Adji et al., 2019; Rahimpour, 2008; Zabiri et al., 2010; Sadeghi et al., 2014; Maksimov et al., 2021; Shahrokhi and Baghmisheh, 2005). However, there are currently no reports that comprehensively simulated both dynamic and steady-state behaviours of methanol reactors while also analysing reactor responses (conversion, temperature, pressure drop, etc.) based on variations of parameters such as bed porosity (ε_{pm}), stoichiometric ratio of hydrogen to carbon (SH), and Gas-Hourly-Space-Velocity (GHSV). Furthermore, no existing studies translate such simulations to both an in-house laboratory-scale digital twin (e.g., Micromeritics reactor) and an industrial-scale reactor. Additionally, there are no reports on the thermostatic regulation of the small-scale reactor, considering that methanol synthesis is exothermic, and the performance of most heterogeneous catalysts is temperature dependent. However, to accurately implement thermostatic regulation, it is essential to account for heat transfer between the reactor and its surroundings (e.g., the reactor wall, and circulating cooling fluids). Therefore, the reactor wall temperature must be adequately modelled. This is important because the reactor wall serves as a non-invasive domain where thermostat sensors can be installed. In most studies (Leonzio and Foscolo, 2020; Rahimpour et al., 2009; Parvasi et al., 2008; Hafeez et al., 2020; Bakhtiary et al., 2024; Adji et al., 2019; Rahimpour, 2008; Zabiri et al., 2010; Sadeghi et al., 2014; Masoudi et al., 2019), the reactor wall temperature has been assumed constant. Literature such as **Maksimov et al.** (Maksimov et al., 2021) applied a simplified model, and others such as **Rahimpour** (Rahimpour, 2008) and **Zhu et al.** (Zhu et al., 2020), implemented more comprehensive approach (as would be used in this work), that involves iterative calculations of the reactor wall temperature based on its thermal interaction with both the reactor contents and the coolant.

The research gaps highlighted in the preceding paragraph form the basis of this study and define its novelty. Accordingly, the aims and

Table 1
Comparison of energy properties of hydrogen, and its renewable fuel derivatives (Palys and Daoutidis, 2022; Amin, 2019; Taccani R, Maggiore G, Micheli D. Development of a Process Simulation Model for the Analysis of the Loading and Unloading System of a CNG Carrier Equipped with Novel Lightweight Pressure Cylinders. Applied Sciences, 2020; lrak.net. Energy density, 2019; U.S. Department of Energy. Alternative Fuels Data Center: Fuel Properties Comparison, 2024).

	Hydrogen	Ammonia	HDRD	Ethanol/E100	Methane	Methanol
Mass energy density (kWh kg^{-1})	33.3	5.2	12.2	7.5	15.4	5.6
Storage pressure at 25 °C (bar)	300 – 700	10	1	1	~250	1
Volumetric energy density (kWh L^{-1})	0.5 – 2.3	4.3	9.5	5.9	~6.4	4.6

HDRD – Hydrogenation-derived renewable diesel. Storage pressure is based on a simple pressure vessel.

objectives of this work are as follows: Evaluate and select adequately reported **Graaf et al.** Langmuir-Hinshelwood-Hougen-Watson (LHHW) type methanol kinetic model; Develop a detailed model for a micro-scaled laboratory reactor, incorporating th the temperature, concentration, and pressure drop profiles along the reactor; Evaluate the dynamic and steady-state reactor responses (conversion, temperature, pressure drop, etc.) under varying conditions of bed porosity, stoichiometric ratio of hydrogen to carbon, reactor diameter, catalyst bed length and Gas-Hourly-Space-Velocity (GHSV), temperature and pressure; Translate the developed model to the scale of an in-house laboratory digital twin (Micromeritics reactor), and an industrial- scale reactor; Evaluate the adequacy of heat transfer processes, and implement thermostat regulation of the reactor temperature. Furthermore, while most reported packed bed reactor models for methanol synthesis applied MATLAB for the numerical simulations, a few studies, such as those by **Bakhtiary et al.** (Bakhtiary et al., 2024) and **Adji et al.** (Adji et al., 2019), applied COMSOL Multiphysics for modelling the process. COMSOL Multiphysics may be preferred over MATLAB because it offers a more user-friendly and specialised platform for solving partial differential equations (PDEs) on complex geometries using the finite element method (FEM) (Wang et al., 2011). It also supports more advanced discretisation techniques beyond the linear method, such as quadratic and higher-order polynomial discretization, which enable more accurate gradient computations. Additionally, COMSOL offers more realistic three-dimensional visual representations of both the reactor system and the simulation results.. Therefore, COMSOL Multiphysics will be used to implement the preceding set of objectives highlighted in this study.

2. Process description of micro-scaled reactor

Fig. 1 illustrates a cylindrical packed bed Micromeritics reactor for methanol synthesis, loaded with a commercial $Cu/ZnO/Al_2O_3$ catalyst. The catalysts are supported by a partitioning mesh to ensure uniform arrangement and accurate measurement of the bed length. The reactor is made of steel, with the inner diameter and wall thickness given in Table 2. A heat exchanger is integrated along the reactor wall to regulate the reaction temperature. The reactant feed stream, comprising of CO, CO_2, H_2, and inert N_2 species, in predefined compositions, is pumped into the reactor at a given Gas hourly space velocity (GHSV).

The average reactor temperature is measured and controlled using spatially distributed sensors, such as K-type thermocouples, positioned along radial domains r (0, 1/2, and 1), i.e., from the centre to the internal surface of the reactor wall. Given the exothermic nature of methanol synthesis reactions, Equation (1) – (3), these temperature sensors, along with a temperature controller (TC), continuously monitor and regulate temperature variations within the reactor. The reactor pressure is monitored and controlled with a back-pressure regulator (PC). Additionally, the reactor outlet is connected to a Gas Chromatography (GC) or Raman cell equipped with a gas-phase Raman probe, which transmits the composition signal to a Raman spectrometer for analyzing the reactor effluent composition.

Table 2
Specification of reactor design details, catalyst, and feed composition.

	Parameters, units	Values
Reactor dimension		
	Inner diameter of reactor, D_{R-i} (mm)	10.000
	Reactor thickness, x_w (mm)	1.0000
	Outer diameter of reactor, D_{R-o} (mm)	$2\,x_w+D_{R-i}$
	Hydraulic diameter of cooling jacket, D_C (mm)	5.0000
	Total length of parent tube, L (mm)	200.00
	Length of catalyst bed, L_{pm} (mm)	150
	Length of reactor inlet section, L_{R-i} (mm)	$0.5(L-L_{pm})$
	Length of reactor outlet section, L_{R-o} (mm)	$L_{R-o}=L_{R-i}$
Catalyst		
	Catalyst density (kg m^{-3})	1450.0
	Bed porosity,ε_{pm}	0.3400
	Catalyst porosity,ε_p	0.2800
	Catalyst radius, r_p (μm)	200.00
Feed composition		
	Stoichiometric ratio of hydrogen-carbon species,SH	1.0000
	CO mole fraction,y_{CO}	0.0000
	CO_2 mole fraction,y_{CO_2}	0.2273
	H_2 mole fraction,y_{H_2}	0.6817
	N_2 mole fraction,y_{N_2}	0.0910

3. Modelling methanol packed bed reactor

3.1. Reaction models

In modelling the packed-bed reactor for methanol synthesis, the equilibrium reaction can be modelled using an entropy-based driving force approach via Gibbs (G) or Helmholtz (A) free energy formulations (Solsvik et al., 2016). The theoretical maximum conversion of CO_2, and CO hydrogenation to methanol typically ranges from ~ 18 – 85 % for 300 – 200°C at 100 bars (Dieterich et al., 2020; Gallucci et al., 2004), based on results derived from Gibbs (G) or Helmholtz (A) free energy approach. However, in practice, the maximum achievable conversion of CO_2, and CO over a catalyst is generally about 25 % (Gallucci et al., 2004; Izbassarov et al., 2021; Lombardelli et al., 2022; Etim et al., 2020;

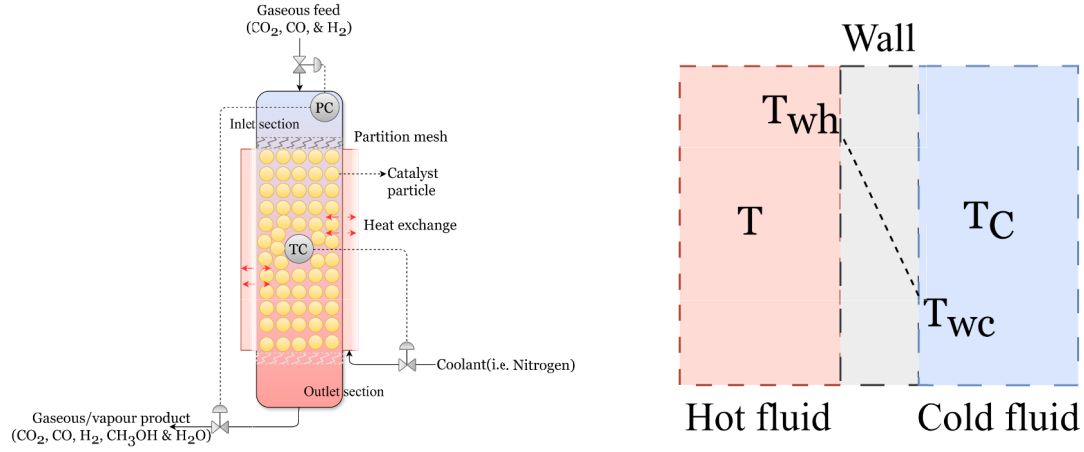

a. Reactor process description b. Temperature gradient across the reactor

Fig. 1. Schematic of Micromeritics reactor for this methanol synthesis.

Table 3
The molar stoichiometric, n_j, for each species of the fluid in the reactor.

Species, j	$r_1 = r_{MEOH-CO}$	$r_2 = r_{MEOH-CO_2}$	$r_3 = r_{RWGS}$
CO	−1	0	1
CO_2	0	−1	−1
H_2	−2	−3	−1
N_2	0	0	0
CH_3OH	1	1	0
H_2O	0	1	1

Sahibzada et al., 1998). As a result, equilibrium-based approaches are often insufficient to fully represent the practical limitations of methanol synthesis. Therefore, the reaction is commonly modeled using rate-based kinetic models, such as the Langmuir–Hinshelwood–Hougen–Watson (LHHW) (Graaf et al., 1988; Vanden and Froment, 1996; Villa et al., 1985; Park et al., 2014; Seidel et al., 2018) and power law models (Peter et al., 2012; Kobl et al., 2016) to better capture the kinetic constraints and catalytic behaviour. Among these rate-based kinetic models, $r_{j=1,2\&3}$(mol kg_{ct}^{-1} s^{-1}), the **Graaf et al.** (Graaf et al., 1988) model, Equation (5) – (8) is an effective, and popularly reported in literature, even in recent years (Maksimov et al., 2021; Slotboom et al., 2020; Nyári et al., 2022). Therefore, it will be adopted to model the reaction kinetics in this study. The models are expressed in terms of the partial pressure (P_j) of the reacting species, j = CO, CO_2, H_2, N_2, CH_3OH, H_2O. These expressions can be categorised into three main components: The adsorption term, θ_*, with K_1, and K_2 (bar^{-1}) as adsorption constants for CO, and CO_2; and K_3 ($bar^{-0.5}$) is a modified adsorption constant to account for the combined effect of H_2O, and H_2 adsorption; The kinetic factor term: with reaction rate constants, K_{P1}, K_{P2}(mol kg_{ct}^{-1} s^{-1} bar^{-1}), and K_{P3}(mol kg_{ct}^{-1} s^{-1} $bar^{-0.5}$); The driving force term, with K_{E1}, and K_{E2} (bar^{-2}) as modified equilibrium constants, and K_{E3} (unitless) is equilibrium constant (Nyári et al., 2022). All constants are temperature-dependent and are expressed using the Arrhenius equation, Equation (A.1) – (A.9), as detailed in the Appendix.

$$r_{MEOH-CO} = \alpha K_{P1} K_1 \left(P_{CO} {P_{H_2}}^{3/2} - \frac{P_{CH_3OH}}{K_{E1} {P_{H_2}}^{1/2}} \right) \theta_* \tag{5}$$

$$r_{MEOH-CO_2} = \alpha K_{P2} K_2 \left(P_{CO_2} {P_{H_2}}^{3/2} - \frac{P_{CH_3OH} P_{H_2O}}{K_{E2} {P_{H_2}}^{3/2}} \right) \theta_* \tag{6}$$

$$r_{RWGS} = \alpha K_{P3} K_2 \left(P_{CO_2} P_{H_2} - \frac{P_{CO} P_{H_2O}}{K_{E3}} \right) \theta_* \tag{7}$$

$$\theta_* = \frac{1}{(1 + K_1 P_{CO} + K_2 P_{CO_2})({P_{H_2}}^{1/2} + K_3 P_{H_2O})} \tag{8}$$

Parameters for the **Graaf et al.** LHHW type model, Equation (5) – (8), based on various literature sources (Graaf et al., 1988; Maksimov et al., 2021; Lombardelli et al., 2022; Khawaja and Usman, 2024; Portha et al., 2017), was simulated and evaluated using data given in Table 2 at GHSV = 2800 h^{-1}. The simulation was based on a one-dimensional model, and the results are presented in Table (A1) and Figure (A1a) – (A1b) of the **Appendix**. It can be inferred that the carbon dioxide conversion and methanol yield (Leonzio G. Methanol Synthesis: Optimal Solution for a Better Efficiency of the Process. Processes, 2018) are within limits reported in literature (Lombardelli et al., 2022). However, in addition to this fact, the **Maksimov et al.** (Maksimov et al., 2021) model and report provided results that can serve as a basis to validate the COMSOL simulated result at 60 bar, and 230 °C, as such, considered more suitable for this study. The results, Table (A2) and Figure (A2) show a slight deviation in the output composition between **Maksimov et al.** (Maksimov et al., 2021) and COMSOL results. This difference is likely due to the distinct simulation methodologies: **Maksimov et al.** (Maksimov et al., 2021) appear to simulate the build-up of reactant compositions (hydrogen and carbon dioxide) from zero to outlet values, rather than the conventional approach of simulating reactant consumption from known initial inlet values (e.g., 68.17 % H_2 and 22.73 % CO_2). Additionally, differences in the one-dimensional modeling framework may contribute to this variation.. Subsequent simulation using a two-dimensional COMSOL model, Section (5), indicates closer agreement with the results of **Maksimov et al.** (Maksimov et al., 2021).

Table 4
Process parameters necessary for the simulation.

Parameter, unit	Value
GHSV (h^{-1}) volume gas per volume catalyst basis	2800.00
Initial/isothermal reaction temperature, T_o,°C	230.000
Initial/reaction pressure, P_o, bar	60.0000
Initial/guess reactor wall temperature, T_w,°C	230.000
Coolant temperature, T_c,°C	20.0000
Initial catalyst activity, α_o (−)	1.00000
Catalyst deactivation constant, K_d (h^{-1})	0.00439
Catalyst deactivation reference temperature, T_d (K)	513.000
Catalyst deactivation energy, E_d (J mol^{-1})	91270.0

3.2. Material and energy model

3.2.1. Concentration balance

In modelling the material and energy balance for the reactor, it is assumed that the concentration and temperature gradient between the fluid and solid phases are negligible. Specifically, Equation (9) governs the molar concentration, C_j (mol m^{-3}) for each reactor species (j = CO, CO_2, H_2, N_2, CH_3OH, H_2O). This continuity equation accounts for the fluid velocity field or Darcy velocity, **u** (m s^{-1}), through the porous solid matrix of porosity, ε_{pm}, with the advection ($\mathbf{u}\nabla C_j$), diffusion ($D_{eff-j}\nabla^2 C_j$), and reactive (R_j(mol m^{-3} s^{-1}) = $\alpha \Sigma n_j r_j \rho_p$) terms considered. Where r_j is the reaction kinetics associated with the three equilibrium reactions, Equation (1) – (3), (i.e., j = 1 = MEOH-CO, 2 = MEOH-CO2, and 3 = RWG), n_j is the reactive molar stoichiometric for each species, Table 3, ρ_p (kg m^{-3}) is the catalyst density, α is catalyst activity, Equation (10) (Keil, 1999; Løvik I. Modelling, estimation and optimization of the methanol synthesis with catalyst deactivation. 126 s, 2001), the definition and values of terms that define α are highlighted in Table 4. The effective diffusivity, D_{eff-j} (m^2 s^{-1}) is deduced from the species diffusivity through the mixture, D_{m-j}, Equation (11), and matrix tortuosity, τ_{pm} (Woods, 2014; Multiphysics, 2024; Wiki and Equation, 2020). Note that in the inlet and outlet sections of the reactor, Fig. 1a, R_j = 0. To solve Equation (9), the following boundary conditions are applied: $C_j(t = 0, r = 0, z = 0) = C_{o-j}$, the Dirichlet condition at the inlet, and $\mathbf{n}(-D_{m-j}\nabla C_j) = 0$, the Neumann condition at the outlet. Given that, C_{o-j} is the initial concentration of species, j, and **n** denotes the outward normal on the boundary.

$$\varepsilon_{pm}\frac{dC_j}{dt} + \mathbf{u}\nabla C_j = D_{eff-j}\nabla^2 C_j + R_j \tag{9}$$

$$\frac{d\alpha}{dt} = -k_d \exp\left[\frac{-E_d}{R}\left(\frac{1}{T} - \frac{1}{T_d}\right)\right]\alpha^5 \tag{10}$$

$$D_{m-j} = \frac{1 - y_j}{\Sigma(y_{j_*}/D_{jj_*})} \tag{11}$$

The diffusivity of binary gases, D_{jj_*} (m^2 s^{-1}), which relates the molar fractions of reactor species, y_{j_*} or y_j are estimated from the Stefan–Maxwell model in COMSOL Multiphysics (Hafeez et al., 2020; Eslamloueyan and Khademi, 2010; Melzi et al.).

3.2.2. Momentum balance

The Brinkman's model, Equation (12), is used to deduce the fluid velocity, u, and/or pressure drop (ΔP) across the porous matrix. It's an

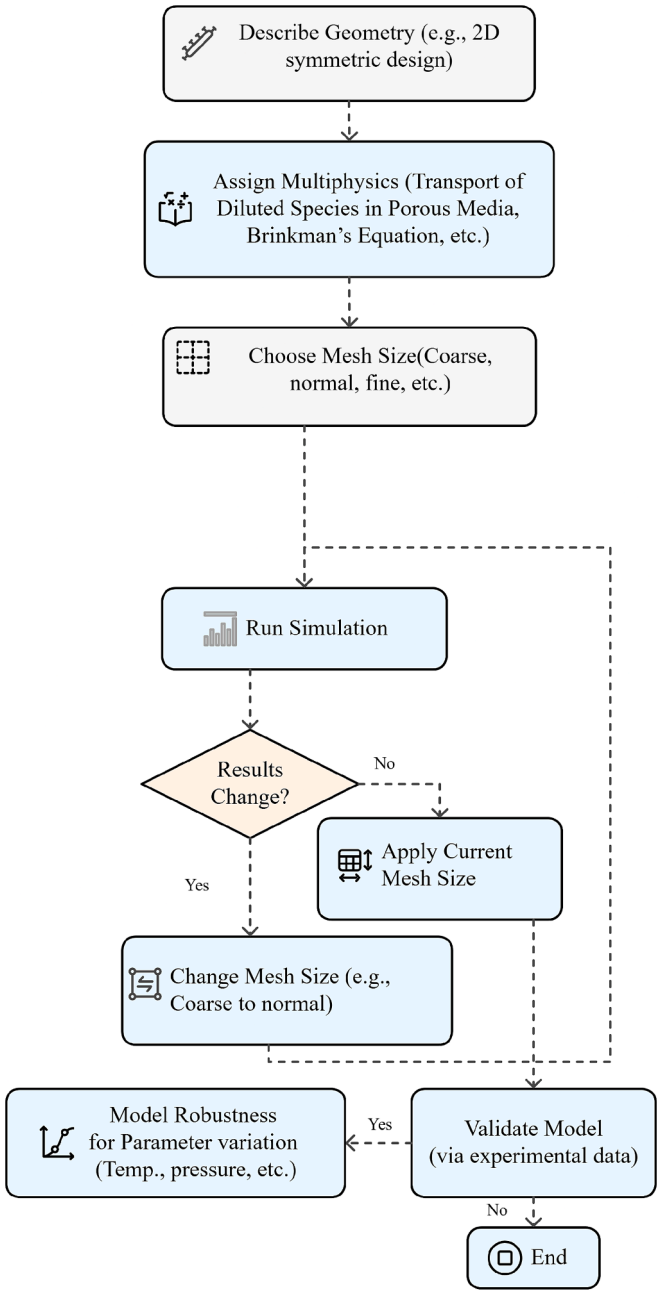

Fig. 2. Schematic of workflow for the modelling and simulation.

expression of fluid density, ρ (kg m^{-3}), dynamic viscosity, μ (kg m^{-1} s^{-1}), matrix permeability, κ (m^2), based on Kozeny–Carman correlation (Modeling, 2020; Xu and Yu, 2008), non-darcy flow coefficient, β (m^{-1}) (Modeling, 2020; Elsanoose et al., 2022), gravity, g (m s^{-2}), and the Forchheimer and Ergun drag viscous force, F (kg m^{-2} s^{-2}), assumed negligible in this study. Where I signifies the identity matrix and the superscript (T) implies transpose.

$$\frac{\rho}{\epsilon_{pm}}\frac{du}{dt} = \nabla.[-PI + k] - \underbrace{\left(\frac{\mu}{\kappa} + \beta\rho|u| + \frac{\nabla(\rho u)}{\varepsilon_{pm}^2}\right)}_{\phi} u + F + \rho g \tag{12}$$

The boundary conditions: u(t = 0, r = 0, z = 0) = u_o, and $[-PI + k]n = -P_o n$, respectively, applies to the reactor inlet and outlet, given that u_o and P_o are known initial fluid velocity and reaction pressure. Where **k** is the viscous stress tensor. Note that in the inlet and outlet sections of the reactor, the "ϕ" term is negligible.

3.2.3. Energy balance

The energy balance for the porous matrix, Equation (13), is a relationship of the effective volumetric heat capacity, $(\rho C_P)_{eff}$ (J m^{-3} K^{-1}), effective thermal conductivity, k_{eff} (W m^{-1} K^{-1}), heat of formation, ΔH_j (J mol^{-1}), reactor temperature, T (K), and reactor hot/inside wall temperature, T_{wh}. Where Q_{R-W}(W) is heat transfer from reactor to its inner wall surface, A_{R-i}, and V_j are the surface area and volume ($j = L_{pm}$) of catalyst bed, h_R(W m^{-2} K^{-1}) is reactor heat coefficient, k, and k_p are fluid and catalyst thermal conductivity, C_P and C_{Pp} (J kg^{-1} K^{-1}) are the fluid and catalyst heat capacities.

$$V_j(\rho C_P)_{eff}\frac{dT}{dt} + V_j\rho C_P u\nabla T = V_j k_{eff}\nabla^2 T + V_j\Sigma\Delta H_j r_j + Q_{R-W} \tag{13}$$

$$V_c\rho_c C_{Pc}\frac{dT_c}{dt} + V_c\rho_c C_{Pc}u_c\nabla T_c = Q_{W-C} - Q_C \tag{14}$$

The temperature boundary conditions applicable to the entire tube containing the Micrometric reactor, Equation (12), are T(t = 0, r = 0, z = 0) = T_o and at the outlet; $-n \bullet (-k\nabla T) = 0$, with T_o being the initial reaction temperature. Note that for the inlet and outlet sections of the reactor, ϵ_{pm}= 0, k_p= 0, C_{Pp}= 0, $\Sigma\Delta H_j r_j$= 0, and necessary space dimensions V_j ($j = L_{R-i}$ or L_{R-o}), Table 2. Furthermore, Equation (14) is the coolant temperature, T_c, i.e., gaseous nitrogen in the cooling tube on the catalyst bed section. The subscript, "c" denotes coolant, V_c is volume of cooling tube, Q_{W-C} is heat transfer from reactor outer wall surface to coolant, A_{R-o} and D_C is cooling tube surface area, and diameter, h_C is the coolant heat coefficient, T_{wc} is the cold/outer wall temperature, Q_C is cooling supplied with q_c as the volumetric flowrate of coolant, and T_c(t = 0) = T_{oc} is the applicable boundary condition.

3.2.4. Computation of heat transfer coefficient

Equations (15) – (16), for packed-bed and cylindrical pipe (Geb et al., 2012; Bavière et al., 2006) are a Nusselt correlation of Reynold number, Re, for reactor content, Re_c is for coolant as well as the Prandtl number, Pr and Pr_c with viscosity correction factor (Bozorgan et al., 2012); to estimate the heat coefficient for reactor, h_R and coolant, h_C, at the reactor, T_f) and coolant, T_{fc} film temperatures through iterative estimation of T_{wh} or T_{wc} by assuming the heat transfer from reactor to hot/inner reactor wall surface, Q_{R-W}, heat transfer from hot to cold/outer reactor wall surface, Q_W, heat transfer from reactor cold wall surface to coolant, Q_{W-C} are all equal, and as such, the overall heat transfer from reactor to coolant, Q_{R-C} are the same. Where, U_i is the overall heat coefficient, Equation (17), $\overline{A}_w$ is the logarithmic area, $\overline{D}_R$ is the reactor logarithmic diameter, and x_w is the reactor wall thickness. Note that the subscript "w" denotes wall, properties such as k_w is considered wall thermal conductivity. Furthermore, μ_{c^*} and μ_{wc} are coolant viscosity at bulk, T_c, and cold wall temperature, T_{wc}.

$$Nu_R = \frac{h_R D_{R-i}}{k} = 0.057Re^{0.96}Pr^{1/3} \tag{15}$$

$$Nu_C = \frac{h_C D_c}{k_c} = 0.0243Re_c^{0.8}Pr_c^{0.4}\left(\frac{\mu_{c^*}}{\mu_{wc}}\right)^{0.14} \tag{16}$$

$$U_i = \frac{1}{\frac{1}{h_R} + \frac{x_w}{k_w}\left(\frac{D_{R-i}}{\overline{D}_R}\right) + \frac{1}{h_C}\left(\frac{D_{R-i}}{D_{R-o}}\right)} \tag{17}$$

4. Model computations and additional parameters

To solve the highlighted time–space partial differential equations, dynamic models combined with analytical and empirical correlations were implemented using the COMSOL Multiphysics Software 6.0 for both steady-state and dynamic simulation. Equation (5) – (11) is

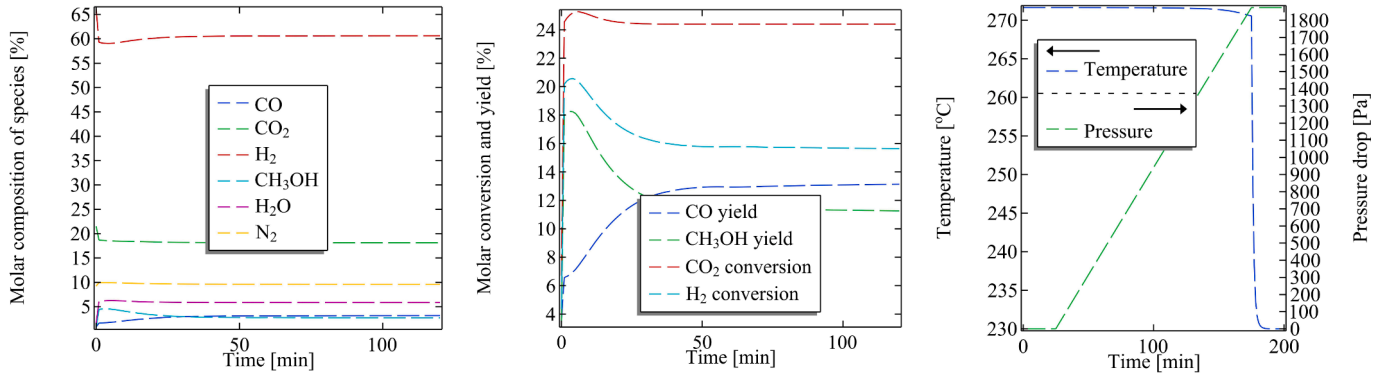

Fig. 3. Dynamic simulation of two-dimensional modelled methanol synthesis Micromeritics reactor.

Table 5
Comparison of Maksimov et al. (Maksimov et al., 2021) and two-dimensional COMSOL simulated results.

Final molar composition (%)	**Maksimov et al.** (Maksimov et al., 2021)	COMSOL
Carbon monoxide	2.400	2.96
Carbon dioxide	19.00	18.2
Hydrogen	62.00	60.5
Methanol	2.500	2.89
Water	5.000	5.85
Nitrogen	9.100	9.60

associated with the "Transport of Diluted Species in Porous Media", Equation (12) with "Brinkman's Equation", Equation (13) with "Heat Transfer in Porous Media", Equation (14) and iterative estimation of wall temperature with "Coefficient form Boundary PDE", in addition to "Event Interface" for thermostatic regulation. Furthermore, the necessary species and mixture properties (i.e., density, viscosity, the heat of formation, specific heat capacity, etc. for j = CO, CO_2, H_2, N_2, CH_3OH, H_2O), along with binary interaction parameters of the mixture, were deduced using the Soave-Redlich-Kwong thermodynamic fluid package inbuilt in COMSOL. The "Material" node via inbuilt components copper (Cu), zinc oxide (ZnO), and aluminium oxide (Al_2O_3) was used to model the Cu/ZnO/Al_2O_3 catalyst/solid porous matrix. The reactor wall was modelled as steel using properties reported in literature (Zarghoon et al., 2024). Further process parameters necessary for the simulation are highlighted in Table 4.

In discretising the model, a linear discretisation scheme was applied to "Transport of Diluted Species in Porous Media", "Heat Transfer in Porous Media", and "Brinkman's Equation" physics nodes. While the quadratic discretization was applied to the "Coefficient form Boundary PDE" and "Event Interface" physics nodes. Furthermore, as highlighted in Figure (A3a), the extremely coarse mesh was applied to the two-dimensional geometry, since no difference in results was observed at further reduced mesh size, i.e., normal coarse mesh, Figure (A3b). Figures (A3a) and (A3b) illustrate the two-dimensional geometry of the Micromeritics reactor, as well as the extremely coarse mesh applied. A summary of the overall modelling and simulation workflow is provided in Fig. 2.

5. Results and discussion

Although the model and experimental data reported by **Maksimov et al.** (Maksimov et al., 2021) was earlier modelled by a one-dimensional approach using the Reaction Engineering node in COMSOL, Table (A2) and Figure (A3). Restimulation using more accurate two-dimensional approach with coupled "Transport of Diluted Species in Porous Media", and "Heat Transfer in Porous Media", "Brinkman Equation", as well as other physic nodes, may be necessary to obtain better results, Fig. 3a, and Table 5, as it simulates more precisely the experimental condition.

The results show that CO_2 conversion of 24.2 %, and methanol yield of 16 % with temperature rising from 230 °C to about 270 °C, as well as a pressure drop across the reactor of about 1900 Pa, Fig. 3a – 3c and Fig. 4a – 4c for dynamic and steady-state simulation. The subsequent molar composition of reactor species, Table 5, especially the molar amount of methanol, is well within limit of the experimental results deduced by **Maksimov et al.** (Maksimov et al., 2021).

Additionally, the results from this COMSOL simulation, Fig. 3a and 4a can also be validated with the observed trends in other similarly reported literature, such as the **Perez-Fortes et al.** (Pérez-Fortes et al.,

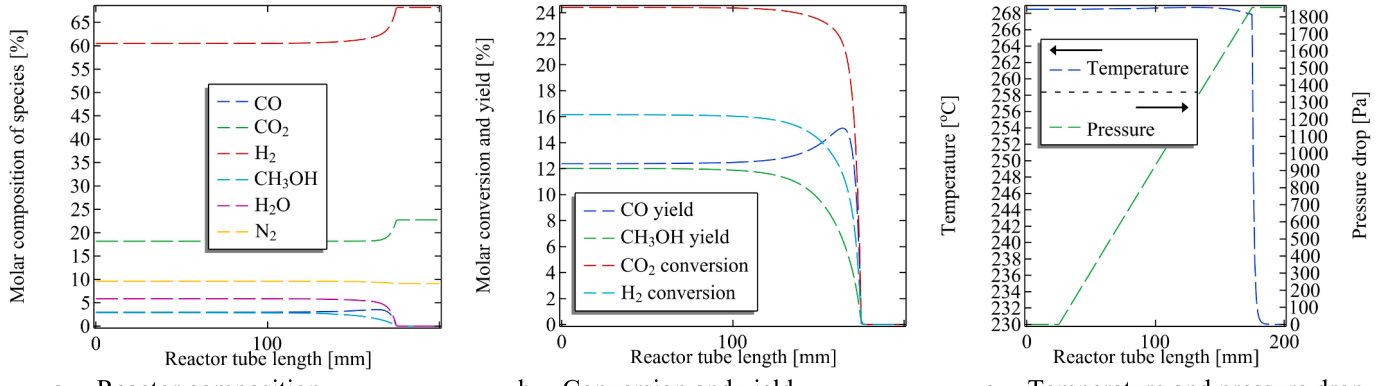

Fig. 4. Steady-state simulation of two-dimensional modelled methanol synthesis Micromeritics reactor.

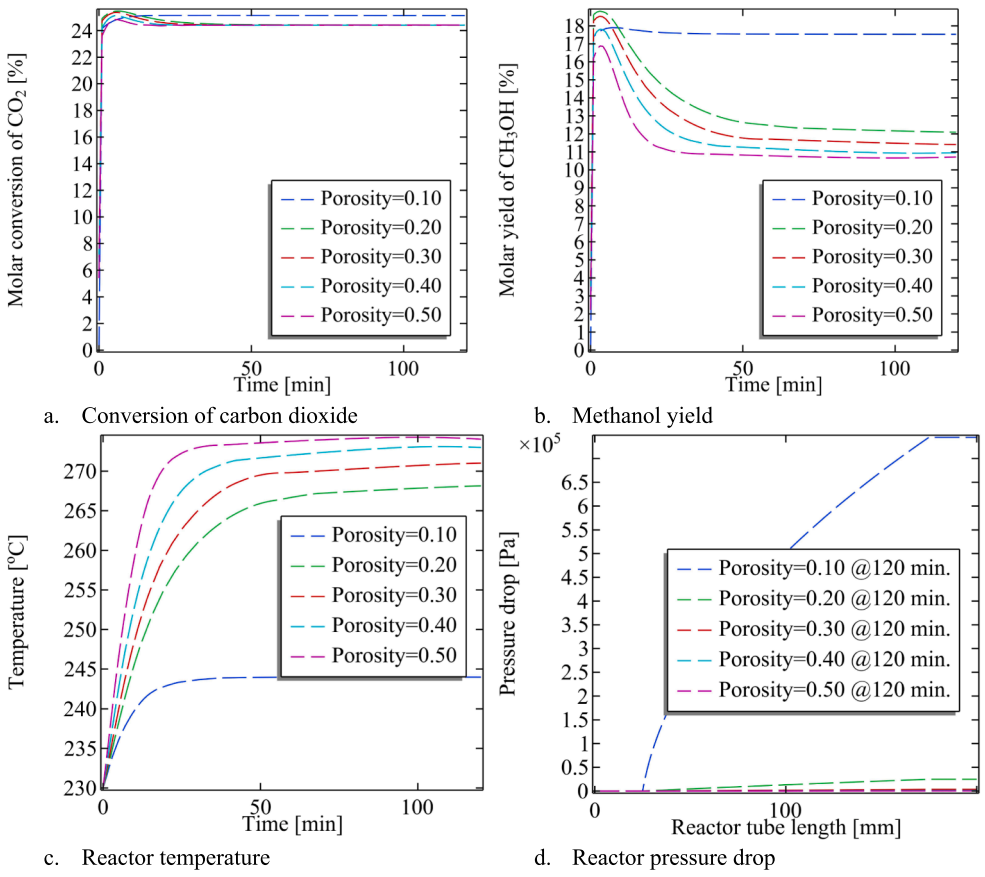

Fig. 5. Results for dynamic simulation of the effect of catalyst bed porosity on reactor responses.

2016) report, which illustrated the volumetric composition of species in an adiabatic ideal plug flow reactor (PFR). And as well as the **Izbassarov et al.** (Izbassarov et al., 2021) report, which illustrated the mass fraction profiles of reactants for the 2D fixed-bed reactor.

Having validated the COMSOL simulation result, it is also necessary to evaluate the model adequacy and assess the optimal operating conditions of key reactor responses, which include carbon dioxide conversion and methanol yield (as indicators of reaction efficiency), temperature, as well as pressure drop profile along the reactor length. This investigation is carried out by examining the influence of catalyst characteristics (i.e., bed porosity), reaction stoichiometry (hydrogen to carbon stoichiometry ratio), Gas-Hourly-Space-Velocity, temperature, and pressure.Fig. 5a – 5d and 6a – 6d present the dynamic and steady-state simulations for varying bed porosity (ε_{pm} = 0.1 – 0.5), at a fixed stoichiometric ratio (SH = 1), Gas-Hourly-Space-Velocity (GHSV = 2800 h^{-1}), initial temperature (230 °C), and reactor pressure (60 bar). The results indicate that bed porosity significantly influences the reactor performance. As anticipated, lower bed porosity leads to higher carbon dioxide conversion, and methanol yield. This is attributed to a more tightly packed catalyst bed, which typically results from smaller average catalyst particle sizes, thereby increasing the number of active catalytic sites available for the reaction. Additionally, a densely packed catalyst bed offers greater catalyst mass, which enhances its capacity to absorb the exothermic heat released during the reaction. This consequently results in a lower reactor temperature, as observed in Fig. 5c and 6c. Conversely, increasing porosity reduces the available catalyst mass, thereby limiting heat absorption, and leads to a rise in reactor temperature. This behavior reinforces the importance of bed porosity optimization for effective thermal regulation and improved methanol synthesis efficiency.

A critical look at the result indicates bed porosity has a nonlinear relationship, especially at $\varepsilon_{pm} < 0.2$. It can be inferred that the hypothesis of more available active sites to catalyse the reaction for lower porosity is quite negligible at ε_{pm} = 0.2 – 0.5, although observable at $\varepsilon_{pm} < 0.2$. This is because CO_2 conversion at ε_{pm} = 0.2 – 0.5 are the same (~24 %), Fig. 5a and 6a, while for ε_{pm} = 0.1, it's about 25 %. However, the methanol yield, Fig. 5b and 6b, is not commensurate with the carbon dioxide conversion. It can be observed that the methanol yield at ε_{pm} = 0.2 – 0.5 increases with lower porosity, unlike for carbon dioxide conversion. Noticeably, as observed for carbon dioxide conversion, the methanol yield for ε_{pm} = 0.1 is significantly different from ε_{pm} = 0.2 – 0.5. Moreover, while the results for methanol yield for dynamic simulation, Fig. 5b, seem quite linearly proportional for ε_{pm} = 0.2 – 0.5, for steady-state simulation, Fig. 6b, the result seems nonlinear with quite a negligible difference for ε_{pm} = 0.2 – 0.3, as well as ε_{pm} = 0.4 – 0.5. Having observed that the inferred hypothesis of increasing active sites with lower porosity is quite negligible at ε_{pm} = 0.2 – 0.5, however results of reactor temperature, Fig. 5c and 6c seem to indicate that methanol yield proportionally corresponds with it. This suggests that although the carbon dioxide conversion for ε_{pm} = 0.2 – 0.5 is about the same; the methanol yield is, however, influenced by temperature, as also reported in literature (Hafeez et al., 2020). Specifically, the result shows that lower reactor temperatures at the given reactor pressure of 60 bar favour the formation of methanol, i.e., Equation (1), and higher temperatures shift the equilibrium towards the formation of carbon monoxide, Equation (2).

Furthermore, as expected, the result of the simulation shows that the lower the bed porosity, the higher the pressure drop across the reactor, Fig. 5d and 6d. This is because, for a tightly loaded catalyst bed, the limiting constraint of fluid flow through the bed will result in a higher force per area to cause the flow of reacting species. Notably, the effect of

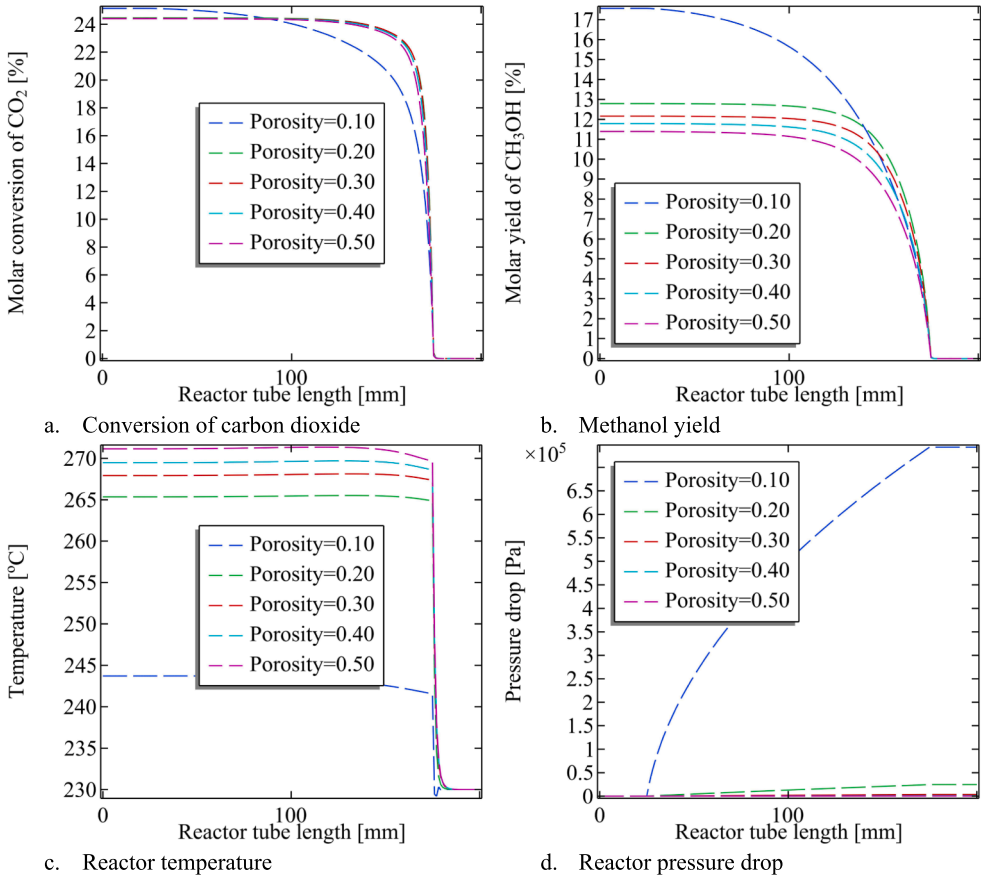

Fig. 6. Results for steady-state simulation of the effect of catalyst bed porosity on reactor responses.

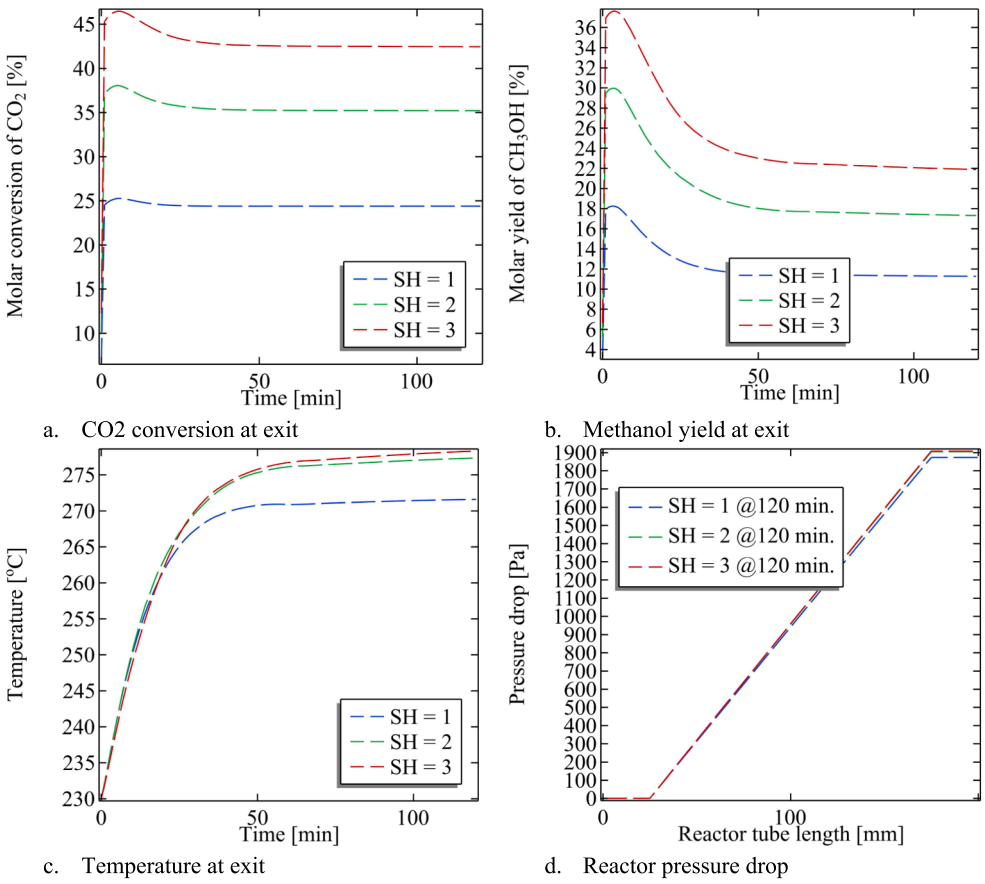

Fig. 7. Results for dynamic simulation of the effect of stoichiometric ratio on reactor responses.

bed porosity on the pressure drops across the reactor, at the end of the dynamic, as well as the steady-state simulation, shows that the influence of bed porosity is highly nonlinear. Although bed porosity (which is proportional to particle size) and the Brinkman equation have been used for the pressure drop calculation, the preceding result is however, similar to that reported by **Zhu et al.** (Zhu et al., 2020) for pressure drop calculation using the Ergun equation for different catalyst particle sizes (0.50 – 2.00 mm).

Fig. 7a – 7d and 8a – 8d, show the dynamic and steady-state simulation of the effect of the stoichiometric ratio of hydrogen-carbon (i.e., SH = 1.00 – 3.00), at catalyst bed porosity (ε_{pm} = 0.34), Gas-Hourly-Space-Velocity (GHSV = 2800 h^{-1}), initial reaction temperature (230 °C), and reactor pressure (60 bar). As expected, the conversion of carbon dioxide, Fig. 7a and 7a, and methanol yield, Fig. 7b and 8b, proportionally increased with increasing stoichiometric ratio of hydrogen-carbon as reported in literature (Takagawa and Ohsugi, 1987). This is because, considering hydrogen is the limiting reactant, the higher the SH, the more active sites on the catalyst are occupied with hydrogen to enhance a higher reaction probability (Gao et al., 2009). However, depending on available active sites on the catalyst, too high an increase in the stoichiometric ratio of hydrogen-carbon can saturate the active site, such that further increase will no longer affect the conversion of carbon dioxide and methanol yield.

Typically, some literature reported the optimal conversion of carbon dioxide and methanol yield at SH < 3.00 (Pérez-Fortes et al., 2016; Bampaou et al., 2021; Xing et al., 2020), while some literature reported optimal value at SH > 3.00 (Collins-Martinez et al., 2013). This disparity in the reported optimal SH is likely due to the nature of the catalyst applied. Specifically, the carbon dioxide conversion is about 25 %, 35 %, and 42 % with corresponding methanol yield of about 12 %, 19 %, and 22 % for SH = 1, 2, and 3, respectively. Although the model can illustrate that increasing SH increases carbon dioxide conversion and methanol yield, however in practice this may be infeasible as the maximum conversion of carbon dioxide is mainly dependent on the type of catalyst applied and is usually around 25 % (Izbassarov et al., 2021; Lombardelli et al., 2022), but may as well increase to as high as 69 % with recycle (Leonzio et al., 2019), which is comparative to the influence of higher SH.

Regarding the reactor temperature, Fig. 7c and 8c. It can be observed that increasing the SH increases the reaction conversion and methanol yield, as such a greater quantity of product species is formed, invariably the greater release of heat energy, and thus the higher the reactor temperature, Fig. 7c – 8c. However, it can be observed that while there is a significant difference in temperature between SH = 1 and 2, the difference between SH = 2 and 3 is quite negligible. Moreover, contrary to the effect of SH on reactor temperature, the effect of SH on pressure drop along the reactor length is quite negligible, Fig. 7d – 8d. This is expected as there is no direct relationship between the SH on the model for pressure drop applied, Equation (10) – (11), rather the slight variation in pressure drop between SH = 1 and SH ≥ 2, is due to volumetric change in gaseous species due to reaction.

Fig. 9a – 9d and 10a – 10d, present the dynamic and steady-state simulation results illustrating the effect of the Gas-Hourly-Space-Velocity (i.e., GHSV = 1400 – 8400 h^{-1}) for a stoichiometric ratio of hydrogen-carbon (SH = 1.00), catalyst bed porosity (ε_{pm} = 0.34), initial reaction temperature (230 °C), and reactor pressure (60 bar). GHSV represents the volumetric amount of reactant species through the catalyst volume. As anticipated, for a given amount of catalyst, GHSV below or within the saturation limit of the catalyst active site coverage will enhance high CO_2 conversion, and subsequently high CH_3OH yield.

However, when the GHSV is well above the saturation limit of the catalyst, a lower conversion of reactant should be expected. Fig. 9a and 9a, specifically illustrate the preceding hypothesis: GHSV = 1400 – 5600 h^{-1}, is likely below or within the saturation limit of the catalyst, unlike GHSV = 8400 h^{-1}, which is well above the saturation limit. This is because the CO_2 conversion for GHSV = 1400, 2800 and 5600 h^{-1} are higher (i.e., 25, 24.4, and 24.2 %) than that of GHSV = 8400 h^{-1} (i.e., 17 %). These findings underscore the critical role of GHSV optimisation. While increasing GHSV can improve throughput, excessive values can hinder conversion efficiency due to mass transfer limitations and reduced catalyst utilization.

Consequently, for GHSV closer to the catalyst saturation limit, the high amount of reactant species consumed will result in high heat of reaction, leading to higher reactor temperature, compared to GHSV well below the saturation limit. This is because a lesser amount of reactant is fed for lower GHSV, and even though high conversion of reactants will also occur, as does when GHSV is closer to the catalyst saturation limit. The corresponding difference in the total amount of reactant consumed in the reaction will cause a difference in reaction temperature. This explains why GHSV = 2800 and 5600 h^{-1} resulted in higher temperatures (i.e., ~ 275 and 268 °C) than GHSV = 1400 h^{-1} with a temperature of about 258 °C. However, for GHSV well above the catalyst saturation limit, the high amount of unreacted species absorbs/dilutes the resulting heat of the reaction, and as such lowers the reactor temperature. This explains why GHSV = 8400 h^{-1} had the lowest temperature(243 °C). Furthermore, apart from GHSV = 8400 h^{-1} with the lowest CO_2 conversion (17 %), as such expected to also result in the lowest CH_3OH yield (6.3 %), Fig. 9b and 10b. GHSV = 1400, 2800, and 5600 h^{-1}, although with similar CO_2 conversion (i.e., 25, 24.4, and 24.2 %), the methanol yield (14.5, 12, 10.5 %) is, respectively, significantly different, due to the influence of reactor temperatures. As earlier inferred, lower temperature favours higher methanol yield. The result for the variation of GHSV = 2800 and 5600 h^{-1} on methanol composition in **Maksimov et al.** (Maksimov et al., 2021) report, validates the result of this simulation, Fig. 9b. Regarding the pressure drop along the reactor, Fig. 9d and 9d, as expected, it can be observed that higher GHSV results in a higher pressure drop. This is because high GHSV also implies high fluid velocity through the porous bed, thus increasing the fluid momentum, nd as such, the reactor pressure.

Fig. 11a – 11d and 12a – 12d, show the dynamic and steady-state simulation of the effect of the reaction pressure (20 – 60 bar) for a Gas-Hourly-Space-Velocity (GHSV = 2800 h^{-1}), stoichiometric ratio of hydrogen-carbon (SH = 1.00), catalyst bed porosity (ε_{pm} = 0.34), and initial reaction temperature (230 °C). In general, the result shows that increasing reaction pressure proportionally increases CO_2 conversion, Fig. 11a and 12a, and CH_3OH yield Fig. 11b and 12b, as well as causes slight changes in the pressure drop across the reactor, Fig. 11d and 12d. The preceding inference on the influence of pressure on CO_2 conversion/ CH_3OH yield conforms with reports from literature (Maksimov et al., 2021; Liu et al., 1996).

Regarding the reactor temperature, it can be observed that increasing reaction pressure enhances reactivity and, as such, increases the reactor temperature, Fig. 11c and 12c. Noticeably, at the lowest pressure of 20 bar for the initial temperature of 230 °C, the lowest CO_2 conversion, and methanol yield are observed, as well as a drop in the reactor temperature. This decrease in temperature could be attributed to the fact that in this condition, the reverse water gas shift reaction, Equation (2), which is endothermic, seems to predominantly prevail,

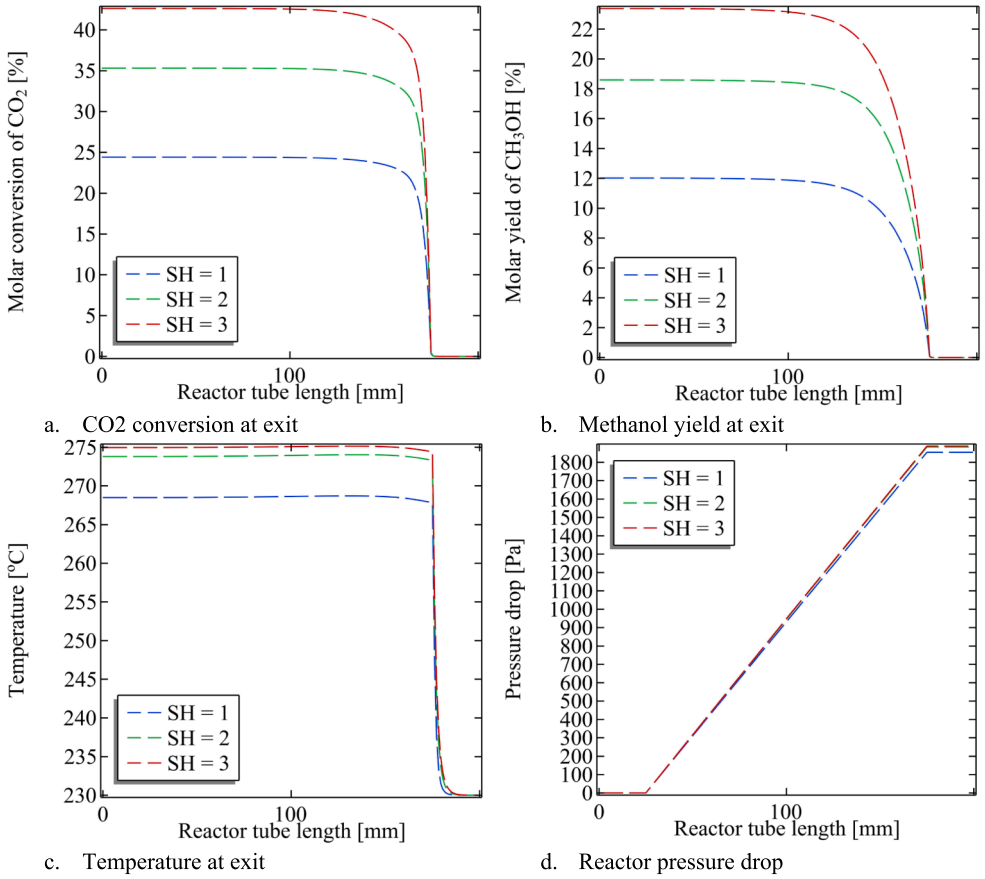

Fig. 8. Results for steady-state simulation of the effect of stoichiometric ratio on reactor responses.

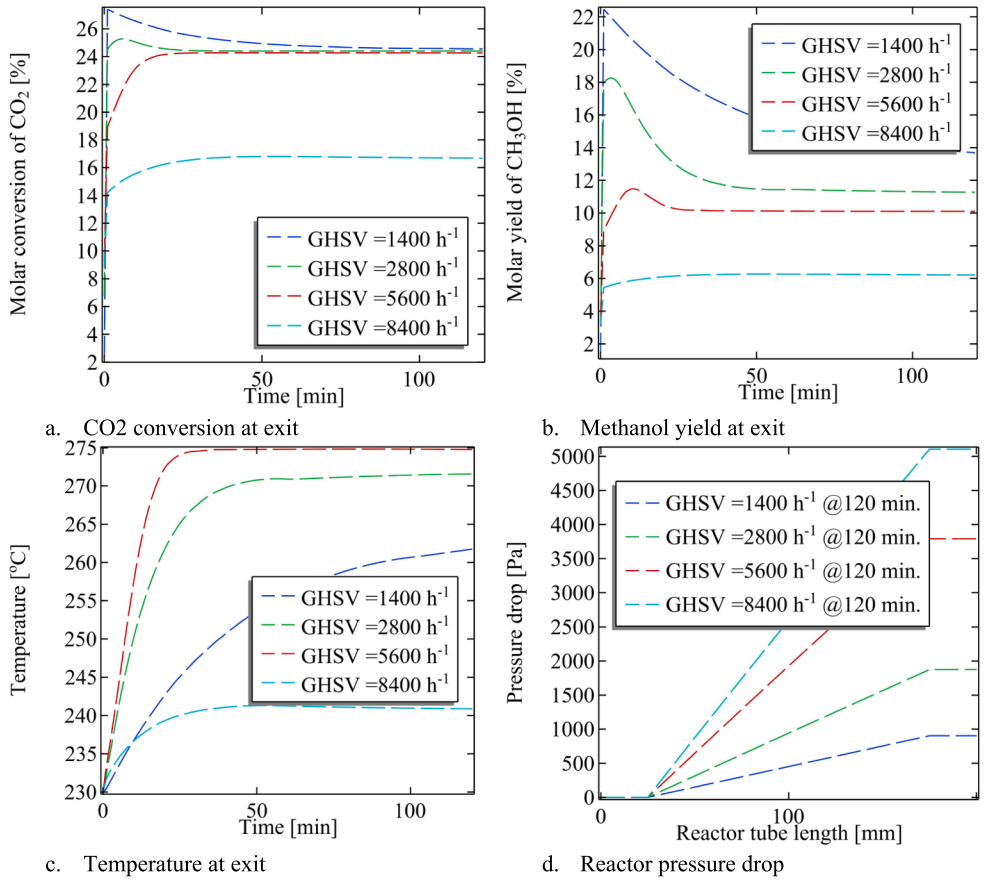

Fig. 9. Results for dynamic simulation of the effect of GHSV on reactor responses.

compared to the exothermic formation of methanol, Equations (1), and (3).

Fig. 13a – 13d and 14a – 14d, show the dynamic and steady-state simulation of the effect of the constant reaction temperature (200 – 280 °C), for a Gas-Hourly-Space-Velocity (GHSV = 2800 h^{-1}), stoichiometric ratio of hydrogen-carbon (SH = 1.00), catalyst bed porosity ($\varepsilon_{pm} = 0.34$), initial reaction temperature (230 °C), and reactor pressure (60 bar). The result shows that reaction temperature within the range of 240 ± 10°C seems to be optimal for the operating pressure. This is because the highest CO_2 conversion and CH_3OH yield occur within this temperature region. Furthermore, it can be observed that CO_2 conversion increases with temperature from 200 °C to 240 °C, after which CO_2 consumption diminishes with further increase in temperature (i.e., 260 – 280 °C in this case), Fig. 13a and 14a. Similarly, the methanol yield also increased with temperature from 200 °C to 240 °C, after which it decreased (i.e., 260 – 280 °C). However, in this case, methanol yield is lower for 260 and 280 °C compared to 220 °C, as opposed to CO_2 conversion for 260 and 280 °C, which is higher than for 220 °C, Fig. 13b and 14b.

Additionally, the variation in reactor temperature is observed to have a negligible effect on the pressure drop across the reactor, Fig. 13c and 14c. The observation of the effect of temperature optimality on CO_2 conversion/CH_3OH yield conforms with the observation from literature (Maksimov et al., 2021; Iyer et al., 2015; Jahanmiri and Eslamloueyan, 2002).

Furthermore, in addition to reaction performance, the heat transfer in the reactor was also elaborately modelled. To evaluate the heat transfer, cooling of the reactor with gaseous nitrogen coolant (20 °C) is initiated, to depict the necessary prevailing assumption that the heat energy through the reactor is conserved, i.e., the heat transfer from reactor to inner wall, Q_{R-W}, heat transfer across reactor wall, Q_W, heat transfer from outer wall to coolant, Q_{W-C} are all equal and as such the same as, Q_{R-C}, Fig. 15b. Which is a necessary assumption used to deduce the heat transfer coefficient of heating, h_R, and cooling, h_C, fluids, Fig. 15c, through the iterative estimation of the reactor wall temperature (i.e., hot, T_{wh} and cold, T_{wc} sides), Fig. 15a.

Having evaluated the adequacy of the heat transfer model through cooling of the Micromeritics reactor, the thermostatic regulation of the reactor temperature within 239 – 241 °C was then implemented using the temperature of the outlet section of the reactor via the Event Interface in COMSOL Multiphysics. The result indicates the reactor temperature, Fig. 16a is adequately within the set limits of the temperature upper and lower bounds, except for the lower bounds, which go to about 239.4 °C. The resulting heat flow between the hot and cooling fluid, Fig. 16b, and heat transfer coefficients for the hot and cool fluid, Fig. 16c, are also highlighted. It can be observed that the heat transfer coefficient for both fluids converge at the upper and lower bounds specified, and heat transfer coefficients of the fluids increase and decrease with temperature as a result of the continuous deviation of reactor temperature from set bounds during regulation by the thermostat within these bounds, thus the reason for the observed oscillatory fluctuation of heat transfer coefficients. While $h_C \cong 1.05\ W\ m^{-2}\ K^{-1}$ for both bounds, h_R varied from 79.9 – 79.7 $W\ m^{-2}\ K^{-1}$ for the lower–upper bound. However, the observed oscillatory fluctuation from these bounds for h_C showed more variation from 0.05 to 2.60$W\ m^{-2}\ K^{-1}$ (i.e., ±100 % changes) in comparison to h_R with 78.8 – 81.4$W\ m^{-2}\ K^{-1}$ (i.e., about ± 1 % changes) throughout the regulation process. This is because the

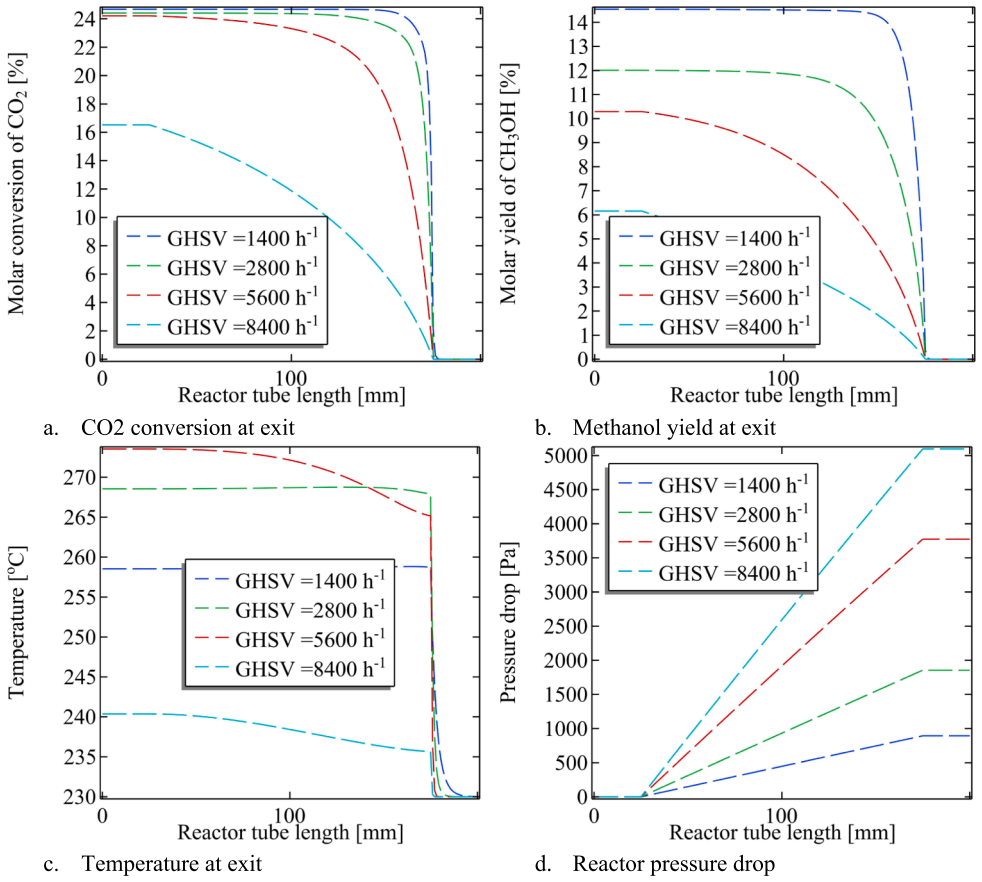

Fig. 10. Results for steady-state simulation of the effect of GHSV on reactor responses.

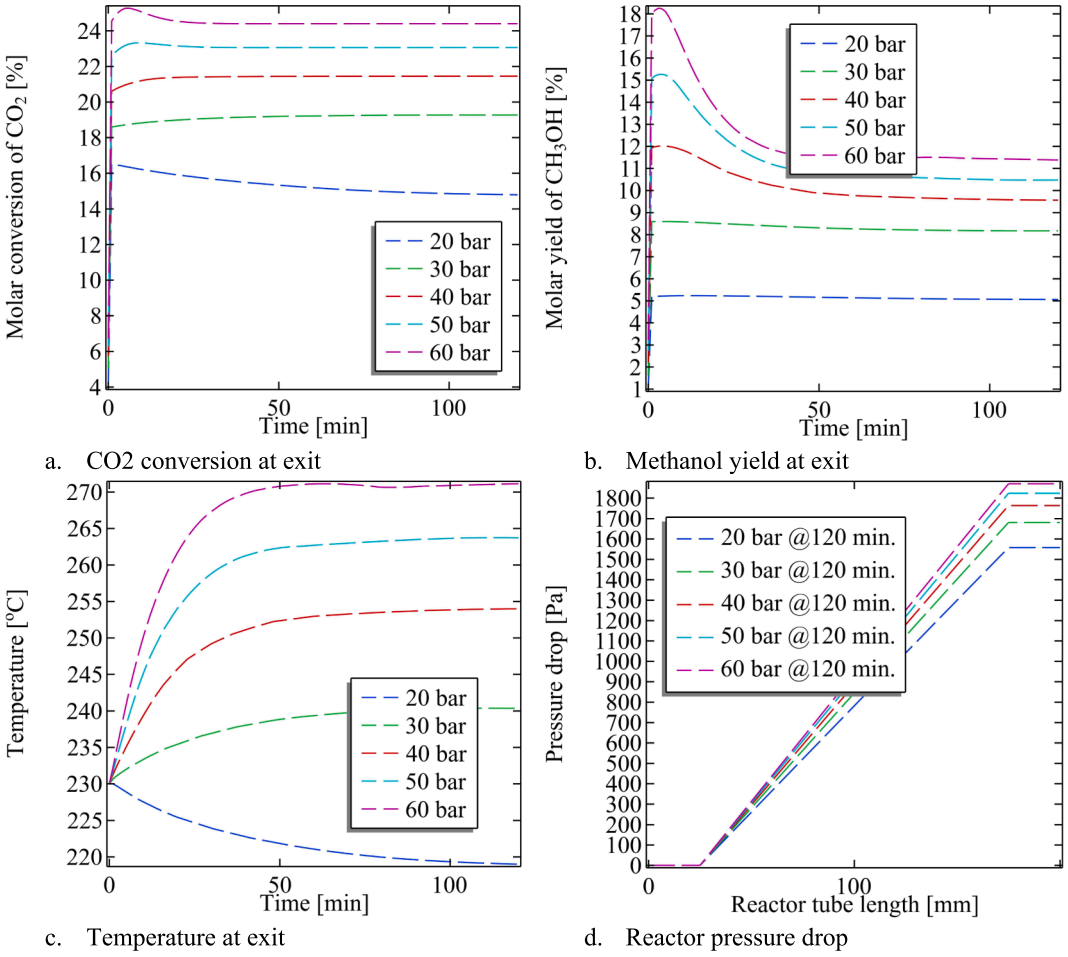

Fig. 11. Results for dynamic simulation of the effect of pressure on reactor responses.

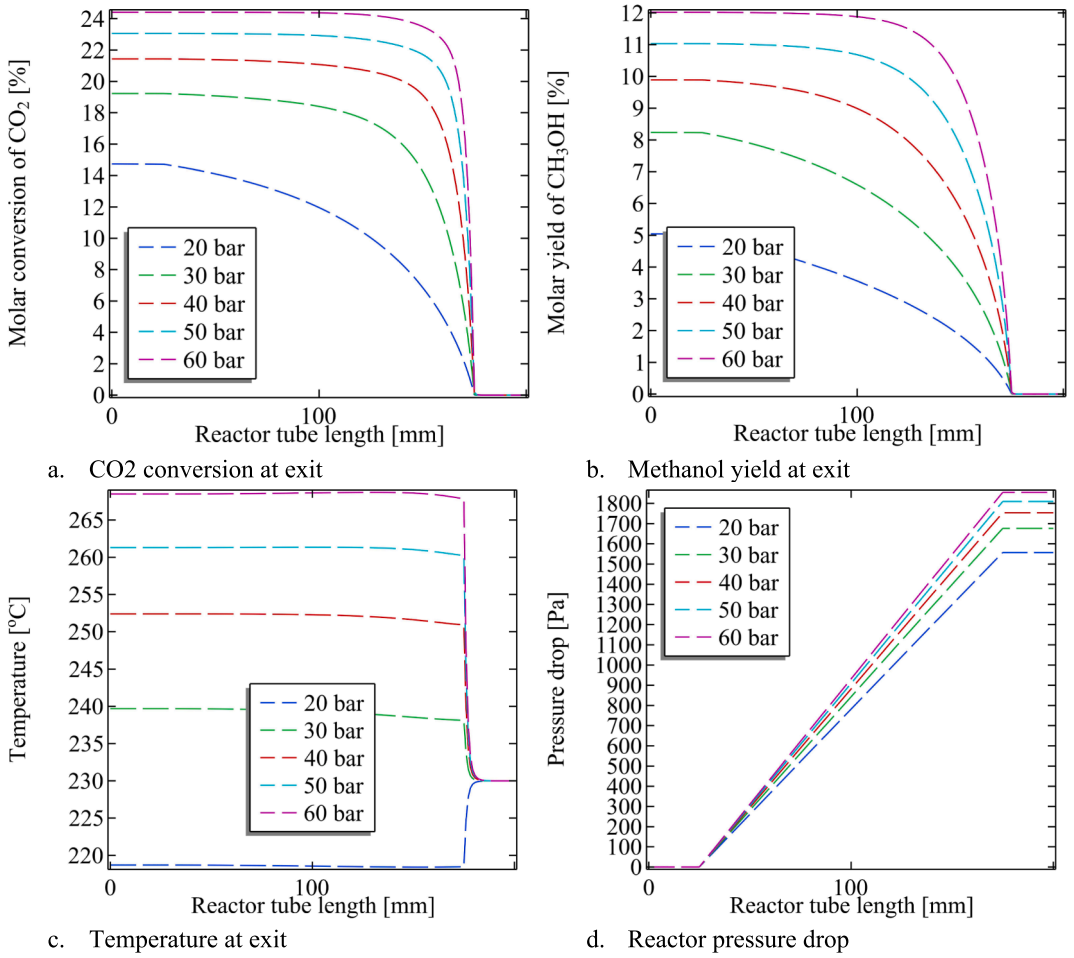

Fig. 12. Results for steady-state simulation of the effect of pressure on reactor responses.

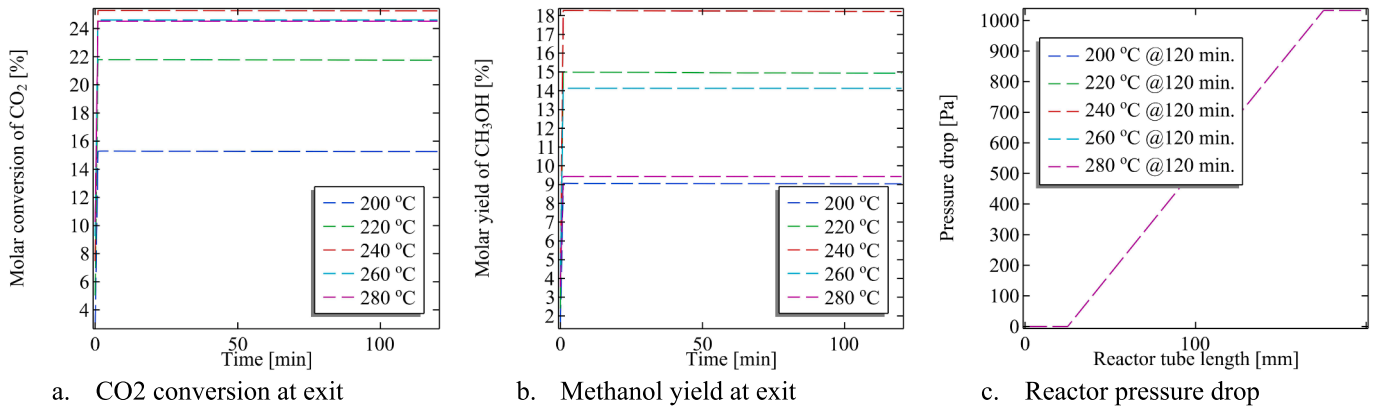

Fig. 13. Results for dynamic simulation of the effect of temperature on reactor responses.

temperature change in the cooling fluid is larger, 20 – 240.5 °C, than the reactor temperature, 239 – 241 °C. In addition to the fact that the specific heat capacity of the coolant (Nitrogen) at standard temperature and pressure is very low in comparison to that of the individual and/or reactants mixture.

Finally, based on the results thus far, it can be observed that the difference between the dynamic and steady-state model/simulation, Figs. 3 – 14, in general, indicates quite a significant difference (i.e., trends) along the catalyst bed. However, the results of the final outlets are quite similar, with a difference of < 2 %. Therefore, either dynamic or steady-state model is adequate to simulate the methanol reactor. As such, based on steady-state simulation, and with the highlighted performance of the simulation thus far, on parameter variations on reactor response. The simulation can be translated into a smaller-scale digital twin of a laboratory Micromeritics reactor, Fig. 17a – 17c, and an industrial-sized reactor, Fig. 18a – 18c. The parameters used for these simulations are highlighted in Table 6, with additional data given in Table 2, except for a negligible amount of nitrogen in the feed stream. The observed difference in reactor content, conversion, and yield from both cases can be attributed to the difference in operating pressure,

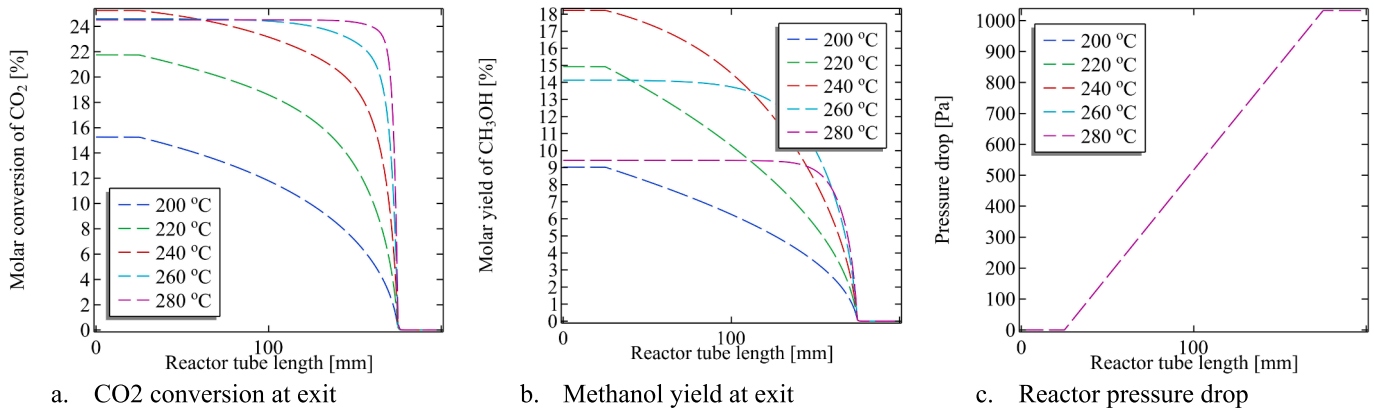

Fig. 14. Results for steady-state simulation of the effect of temperature on reactor responses.

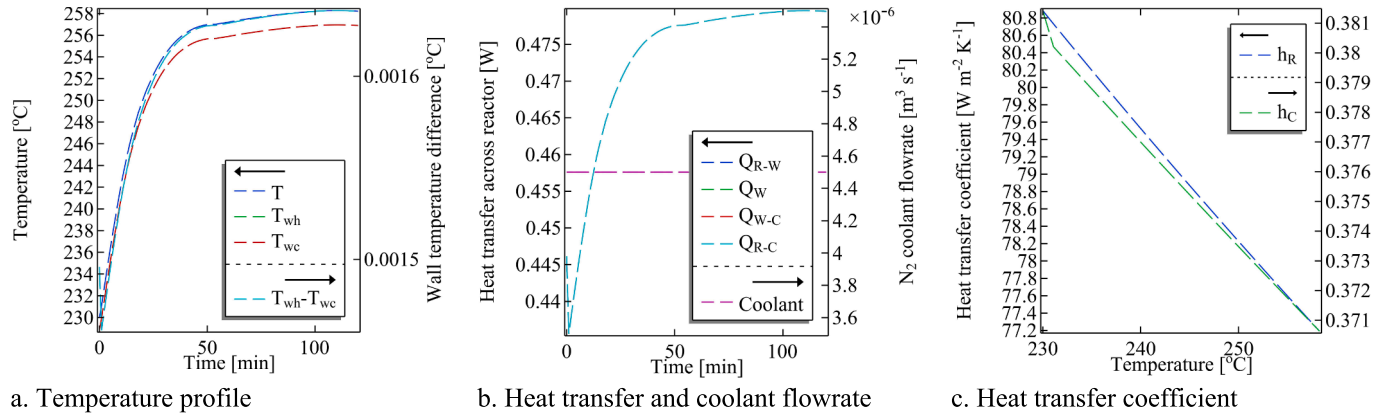

Fig. 15. Dynamic simulation of heat transfer phenomenon across the reactor.

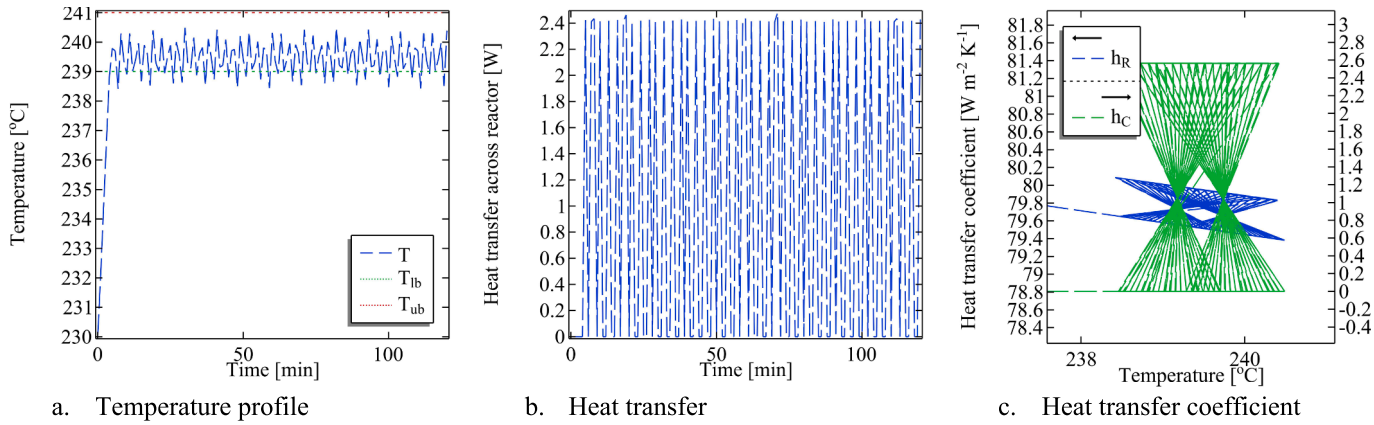

Fig. 16. Dynamic simulation of thermostatic regulation of reactor temperature.

initial temperature, and GHSV, following the preceding inferences for these parameters. Noticeably, it can be observed that the laboratory reactor operated at a higher GHSV of 2273 h^{-1}, due to its shorter length, as opposed to 1400 h^{-1} for the single-tube industrial-sized reactor with a longer length. This is because too high GHSV for a longer packed bed increases its pressure drop significantly, such that it can exceed the reactor operating pressure, and cause problems.

6. Conclusion

In conclusion, a porous-based Micromeritics reactor for methanol synthesis was designed via a Langmuir-Hinshelwood-Hougen-Watson (LHHW) type kinetic model, in addition to adequate modelling heat transfer across the reactor, as well as the thermostat regulation of reactor temperature (239 – 241 °C) was implemented via the Event Interface node in COMSOL Multiphysics. A two-dimensional reactor design with coupled physics node: Transport of Diluted Species in Porous Media; Heat Transfer in Porous Media; Brinkman Equation Interface, etc. were simulated for both dynamic and steady-state conditions, compared and validated with experimentally deduced model, as well as operation conditions (i.e., 60 bar, 230 °C, etc.) reported in literature. Having validated the COMSOL simulated result, the adequacy

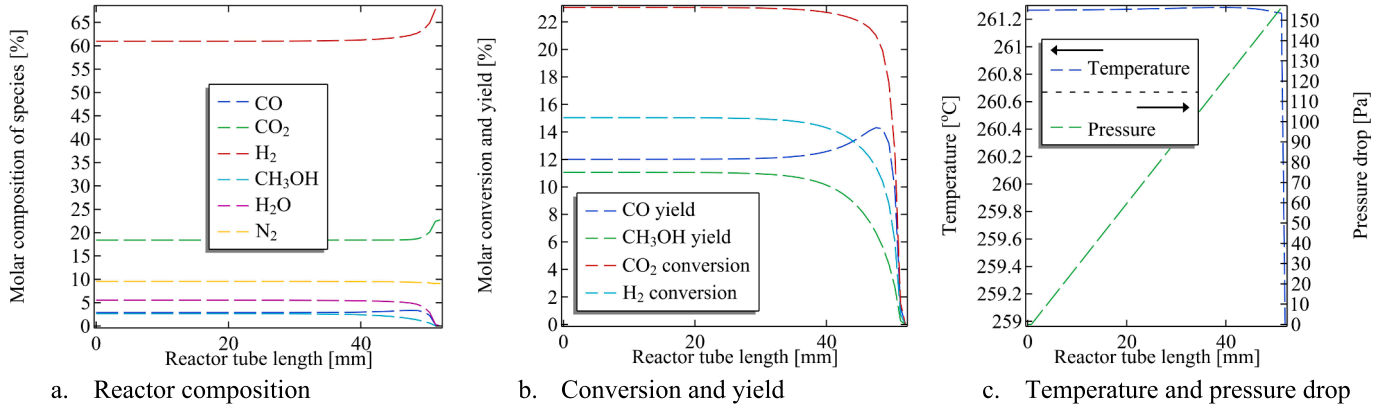

Fig. 17. Steady-state simulation of two-dimensional in-house digital twin Micromeritics reactor.

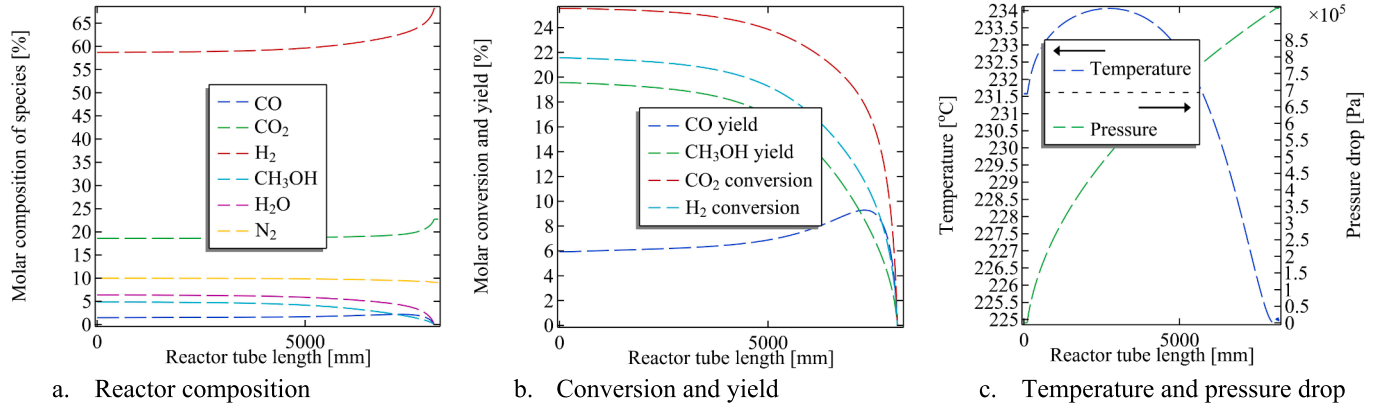

Fig. 18. Steady-state simulation of two-dimensional single-tube industrial-sized reactor for methanol synthesis.

Table 6
Specification of reactor design details, and reaction conditions (Rashid, 2023; Leonzio and Foscolo, 2020).

Parameter	Digital twin Micromeritics reactor	Industrial-sized reactor
Inner diameter, D_{R-i} (mm)	9.120	50.80
Total length of parent tube, L (mm)	52.00	8200
Length of catalyst bed, L_{pm} (mm)	50.52	8000
Reactor wall thinkness, x_w (mm)	1.000	2.000
Bed porosity, ε_{pm} (−)	0.340	0.450
Initial temperature (°C)	240.0	225.0
Pressure (bar)	50.00	55.00

and/or optimal operating conditions of important reactor responses (i.e., carbon dioxide conversion, methanol yield, reactor temperature, and pressure drop) were evaluated by varying the bed porosity ($\varepsilon_{pm} = 0.1 - 0.5$), hydrogen to carbon stoichiometry ratio (SH = 1 – 3), Gas-Hourly-Space-Velocity (GHSV = 1400 – 8400 h^{-1}), reactor temperature, and pressure drop. It was observed that with lower bed porosity, a nonlinear increase in reaction performance occurred, especially for $\varepsilon_{pm} < 0.2$, where the highest carbon dioxide conversion and methanol yield were recorded. Contrary to porosity, increasing hydrogen to carbon stoichiometry ratio increases carbon dioxide conversion and methanol yield to as high as 43 % and 24 % at SH = 3, which may be obtainable in practice by incorporating recycling of unreacted streams, which can be thought to be comparable to the influence of higher SH. It was observed that lower Gas-Hourly-Space-Velocity ensures adequate consumption of carbon dioxide and methanol yield, especially for a GHSV well below the saturation limit of the catalyst active site coverage. Regarding reaction pressure, it was observed that reaction performance increased with increasing reactor pressure at a reactor temperature of 230 °C. While at the reactor pressure of 60 bar, varying the reactor at constant temperatures from 200 °C until 240 ± 10°C, enhances carbon dioxide conversion, after which it can be observed that the reaction performance declines, thus suggesting the optimal temperature is within this range. Furthermore, to the evaluation of reaction performance, the heat transfer in the reactor was also elaborately modelled, and a thermostatic regulator via gaseous coolant nitrogen was used to regulate the reactor temperature. Finally, based on the adequacy of the model, the model was simulated for a smaller-scale digital twin Micromeritics reactor, and for a single-tube industrial-sized reactor. And the results showed that while low to high GHSV can be applied to Micromeritics reactor, low GHSV is required for industrial-sized reactors, due to the effect of pressure drop. Therefore, the findings of the work can serve as a basis for accurate design, sizing, and cost estimation of industrial-sized methanol reactors.

CRediT authorship contribution statement

Samuel Emebu: Writing – original draft, Resources, Methodology, Funding acquisition, Conceptualization, Writing – review & editing, Software, Project administration, Investigation, Formal analysis. **Esko Juhani Lahdenpera:** Writing – review & editing, Software, Visualization. **Michael Chukwuemeka Ekwonu:** Visualization, Writing – review & editing, Validation. **Ibrahim Shaikh:** Visualization, Conceptualization, Writing – review & editing, Project administration. **Arto Laari:** Visualization, Resources, Supervision. **Ojeaga Imanah:** Visualization,

Writing – review & editing, Validation. **Nima Rezaei:** Validation, Writing – review & editing, Resources. **Kim Dong:** Visualization, Supervision, Validation. **Tuomas Koiranen:** Supervision, Conceptualization, Writing – original draft, Formal analysis.

Declaration of competing interest

The authors declare that they have no known competing financial interests or personal relationships that could have appeared to influence the work reported in this paper.

Appendix 1

As generally obtainable for the LHHW reaction rate model, $r_{j=1,2\&3}$(mol.kg^{-1}.s^{-1}), Equation (5) – (8), with defined adsorption term, θ_*, and other factors are defined by Arrhenius models, Equation (A.1) – (A.9), i.e., Adsorption constants: K_1, K_2 and $K_3 = K_{3a}/K_{3b}^{0.5}$; Reaction rate constant: K_{P1}, K_{P2}(mol kg$_{ct}^{-1}$ s^{-1} bar^{-1}), and K_{P3}(mol kg$_{ct}^{-1}$ s^{-1} bar$^{-0.5}$), as well as the equilibrium constants, K_{E1}, K_{E2} and K_{E3}. Where R and T are the ideal gas constant 8.3145 (J mol^{-1} K^{-1}), and temperature (K).

Reaction rate constant:

$$K_{P1} = 0.8303\exp\left(-\frac{32200[\mathrm{J\,mol^{-1}}]}{RT}\right) \tag{A1}$$

$$K_{P2} = 0.1957\exp\left(-\frac{25400[\mathrm{J\,mol^{-1}}]}{RT}\right) \tag{A2}$$

$$K_{P3} = 32400\exp\left(-\frac{64700[\mathrm{J\,mol^{-1}}]}{RT}\right) \tag{A3}$$

Equilibrium constants:

$$K_{E1} = 10^{-12.621+5139[\mathrm{K}]/T} \tag{A4}$$

$$K_{E2} = K_{E1}K_{E3} \tag{A5}$$

$$K_{E3} = 10^{2.029-2073[\mathrm{K}]/T} \tag{A6}$$

Adsorption constants for CO, CO_2, H_2O, and H_2:

$$K_1 = 5.10 \times 10^{-4}\exp\left(\frac{13400[\mathrm{J\,mol^{-1}}]}{RT}\right) \tag{A7}$$

$$K_2 = 4.90 \times 10^{-2}\exp\left(\frac{1260[\mathrm{J\,mol^{-1}}]}{RT}\right) \tag{A8}$$

$$K_3 = 3.18 \times 10^{-10}\exp\left(\frac{101000[\mathrm{J\,mol^{-1}}]}{RT}\right) \tag{A9}$$

The Table (A1) and Figure (A1a) – (A1b) are the results for a one-dimensional COMSOL Multiphysics simulated comparison of different experimentally fitted Graaf et al. LHHW type model, Equation (5) – (8), from reported literature, based on data given in Table 2 with GHSV = 2800 h^{-1}.

Table A1
Comparison of experimental fitted Graaf et al. LHHW type model at 60 bar and 230 °C.

Reported model	Applicable condition	% CO2 conversion	% CH3OH yield	Applicability for simulation
Original Graaf et al. (Graaf et al., 1988)	15 – 50 bar & 210 –245 °C.	~27.52 %	~22.67 %	Yes
Refitted (Maksimov et al., 2021)	20 – 60 bar & 210 –270 °C.	~27.52 %	~22.66 %	Yes
Refitted (Portha et al., 2017)	50 – 80 bar & 200 –230 °C.	~24.64 %	~24.64 %	Yes
Refitted (Lombardelli et al., 2022)	30 – 68 bar & 250 °C.	~27.52 %	~22.66 %	Yes
Refitted (Khawaja and Usman, 2024)	50 bar & 210 –270 °C.	~27.44 %	~22.61 %	Yes

Note that the result for Portha et al. (Portha et al., 2017) was obtained with a slight correction for the equilibrium constant of K_{E3}; Equation (A6), which may have been a typo error in the constant value of the exponent (i.e., 2.029) as reported by Graaf et al. (Graaf et al., 1988) instead of −2.029 as reported by Portha et al. (Portha et al., 2017).

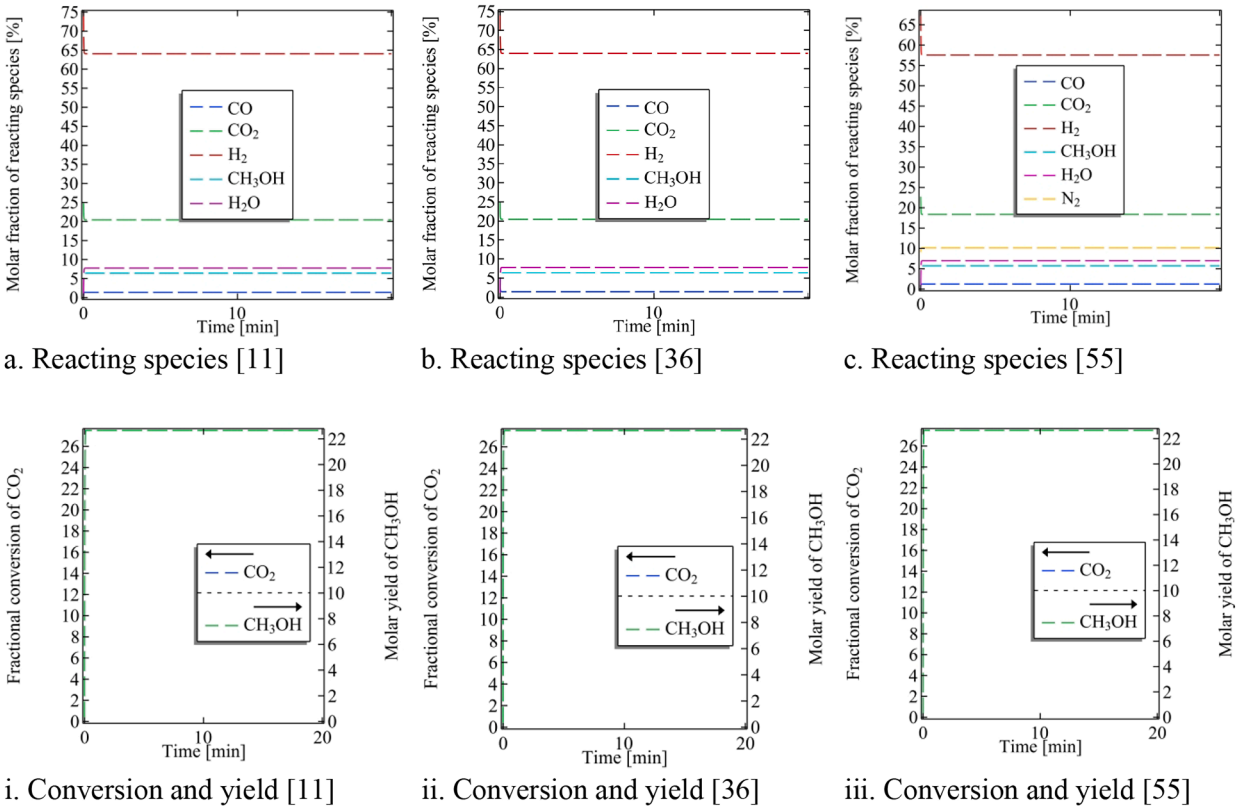

a. Reacting species [11] b. Reacting species [36] c. Reacting species [55]

i. Conversion and yield [11] ii. Conversion and yield [36] iii. Conversion and yield [55]

Fig. A1a. Different simulated experimental Graaf et al. LHHW type models at 60 bar and 230 °C

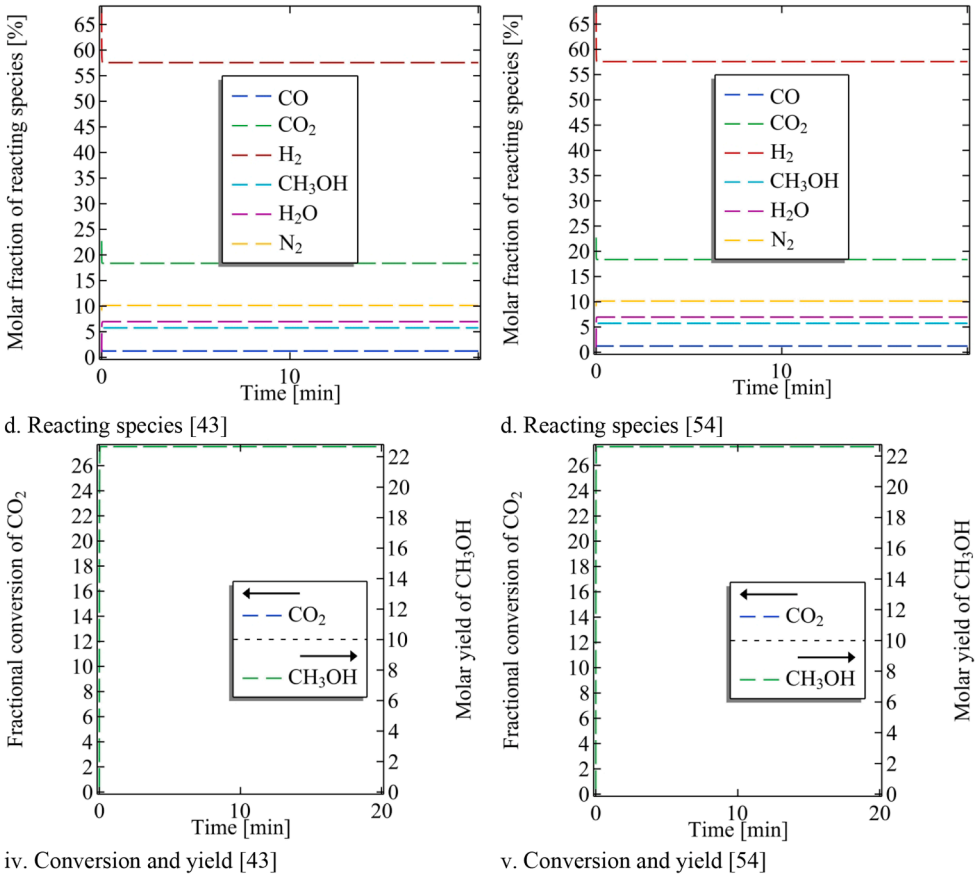

d. Reacting species [43] d. Reacting species [54]

iv. Conversion and yield [43] v. Conversion and yield [54]

Fig. A1b. Different simulated experimental Graaf et al. LHHW-type models at 60 bar and 230 °C

Table A2
Comparison of Maksimov et al. (Maksimov et al., 2021) and COMSOL simulated results.

Exit molar composition (%)	**Maksimov et al.** (Maksimov et al., 2021)	COMSOL
Carbon monoxide	2.400	1.230
Carbon dioxide	19.00	18.37
Hydrogen	62.00	57.57
Methanol	2.500	5.730
Water	5.000	6.960
Nitrogen	9.100	10.14

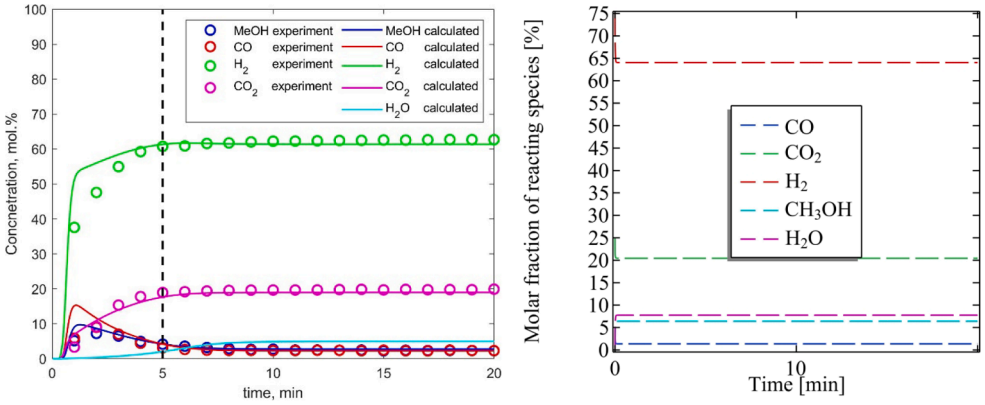

a. **Maksimov et al.** [36] result b. COMSOL simulated result

Fig. A2. Comparison of **Maksimov et al.** (Maksimov et al., 2021) with COMSOL simulated results

Figure (A3b) highlights the two-dimensional discretisation of the extremely coarse mesh applied to the geometry of the Micromeritics reactor, Figure (A3a).

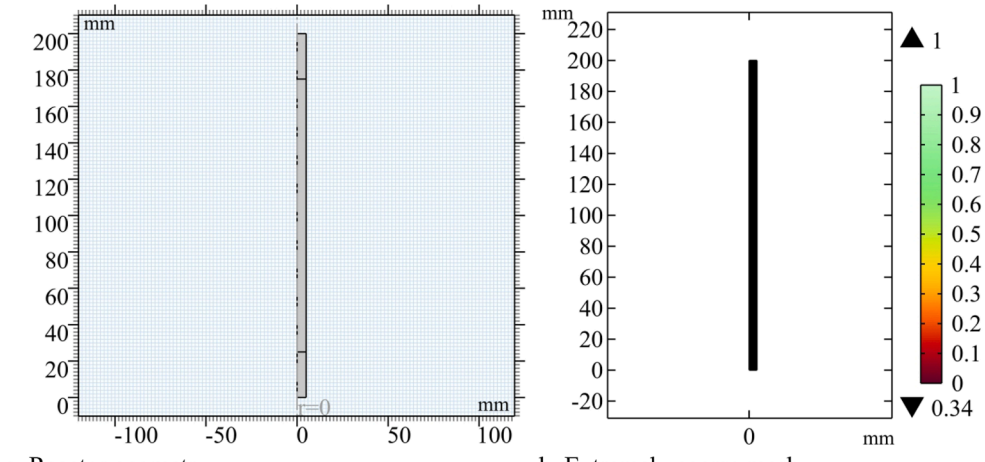

a. Reactor geometry b. Extremely coarse mesh

Fig. A3. Illustration of discretisation mesh applicable to the reactor geometry

Figure (A3) shows the comparison of results between extremely coarse and normal mesh, based on the composition of the reactor at steady-state, and the result shows no difference. Therefore, it implies that the extremely coarse mesh can be used for simulation to reduce computational time.

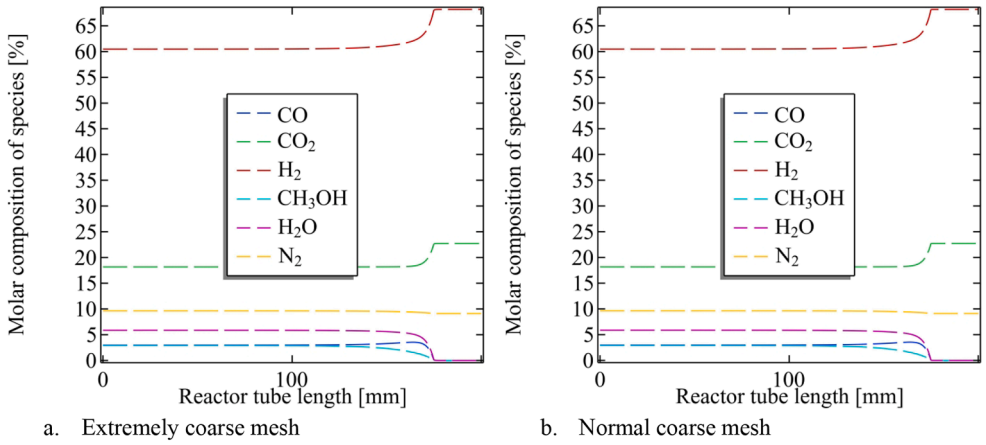

Fig. A4. Comparison of reactor composition at different mesh for steady-state simulation

In general, Equations (9), (12) – (14) respectively express the gradient, $\nabla\Phi$, Equation (A10), and Laplace equation or Laplacian, $\nabla^2\Phi$, Equation (A11), for cylindrical coordinates $\Phi(r, \theta, z)$ with r, θ, and z being the radial, azimuthal, and vertical coordinates of the cylinder. Where Φ represents quantities such as concentration, pressure, temperature, etc. (Curl, Divergence, and gradient in cylindrical and spherical coordinates) and $e_{i=r,\theta,z}$ is the unit vector field that represents the standard orthonormal basis in the cylindrical coordinates.

$$\nabla\Phi = \frac{d\Phi}{dr}e_r + \frac{1}{r}\frac{d\Phi}{d\theta}e_\theta + \frac{d\Phi}{dz}e_z \text{(A10)}.$$

$$\nabla^2\Phi = \frac{1}{r}\frac{d}{dr}\left(r\frac{d\Phi}{dr}\right) + \frac{1}{r}\frac{d^2\Phi}{d\theta^2} + \frac{d^2\Phi}{dz^2} \text{(A11)}.$$

Data availability

No data was used for the research described in the article.

References

International Energy Agency (IEA). Massive expansion of renewable power opens door to achieving global tripling goal set at COP28 2024. https://www.iea.org/news/massive-expansion-of-renewable-power-opens-door-to-achieving-global-tripling-goal-set-at-cop28 (accessed July 7, 2024).

International Energy Agency (IEA). Solar PV 2023. https://www.iea.org/energy-system/renewables/solar-pv (accessed July 7, 2024).

Vaziri Rad, M.A., Kasaeian, A., Niu, X., Zhang, K., Mahian, O., 2023. Excess electricity problem in off-grid hybrid renewable energy systems: a comprehensive review from challenges to prevalent solutions. Renew. Energy 212, 538–560. https://doi.org/10.1016/J.RENENE.2023.05.073.

O'Shaughnessy, E., Cruce, J.R., Xu, K., 2020. Too much of a good thing? Global trends in the curtailment of solar PV. Sol. Energy 208, 1068–1077. https://doi.org/10.1016/J.SOLENER.2020.08.075.

Ince, A.C., Colpan, C.O., Hagen, A., Serincan, M.F., 2021. Modeling and simulation of Power-to-X systems: a review. Fuel 304, 121354. https://doi.org/10.1016/J.FUEL.2021.121354.

Palys, M.J., Daoutidis, P., 2022. Power-to-X: a review and perspective. Comput. Chem. Eng. 165, 107948. https://doi.org/10.1016/J.COMPCHEMENG.2022.107948.

Amin, A., 2019. Review of diesel production from renewable resources: Catalysis, process kinetics and technologies. Ain Shams Eng. J. 10, 821–839. https://doi.org/10.1016/J.ASEJ.2019.08.001.

Taccani R, Maggiore G, Micheli D. Development of a Process Simulation Model for the Analysis of the Loading and Unloading System of a CNG Carrier Equipped with Novel Lightweight Pressure Cylinders. Applied Sciences 2020, Vol 10, Page 7555 2020;10:7555. https://doi.org/10.3390/APP10217555.

lrak.net. Energy density 2019. https://lrak.net/wiki/Energy_density.html (accessed July 7, 2024).

U.S. Department of Energy. Alternative Fuels Data Center: Fuel Properties Comparison 2024. https://afdc.energy.gov/fuels/properties (accessed July 7, 2024).

Graaf, G.H., Stamhuis, E.J., Beenackers, A.A.C.M., 1988. Kinetics of low-pressure methanol synthesis. Chem. Eng. Sci. 43, 3185–3195. https://doi.org/10.1016/0009-2509(88)85127-3.

Nestler, F., Schütze, A.R., Ouda, M., Hadrich, M.J., Schaadt, A., Bajohr, S., et al., 2020. Kinetic modelling of methanol synthesis over commercial catalysts: a critical assessment. Chem. Eng. J. 394, 124881. https://doi.org/10.1016/J.CEJ.2020.124881.

Stangeland, K., Li, H., Yu, Z., 2020. CO2 hydrogenation to methanol: the structure–activity relationships of different catalyst systems. Energy Ecol. Environ. 5, 272–285. https://doi.org/10.1007/S40974-020-00156-4/TABLES/4.

Emebu, S., Martinez, C.M., Omoregbe, O., Mankonen, A., Ogbuoji, E.A., Shaikh, I., et al., 2023. Design, techno-economic evaluation, and optimisation of renewable methanol plant model: Finland case study. Chem. Eng. Sci. 278, 118888. https://doi.org/10.1016/J.CES.2023.118888.

Borisut, P., Nuchitprasittichai, A., 2019. Methanol Production via CO2 Hydrogenation: Sensitivity Analysis and Simulation—Based Optimization. Front. Energy Res. 7, 464607. https://doi.org/10.3389/FENRG.2019.00081/BIBTEX.

Ledakowicz, S., Nowicki, L., Petera, J., Nizioł, J., Kowalik, P., Gołębiowski, A., 2013. Kinetic characterisation of catalysts for methanol synthesis. Chemical and Process Engineering - Inzynieria Chemiczna i Procesowa 34, 497–506. https://doi.org/10.2478/CPE-2013-0040.

Nielsen, N.D., Thrane, J., Jensen, A.D., Christensen, J.M., 2020. Bifunctional Synergy in CO Hydrogenation to Methanol with Supported Cu. Catal Letters 150, 1427–1433. https://doi.org/10.1007/S10562-019-03036-7/METRICS.

Dieterich, V., Buttler, A., Hanel, A., Spliethoff, H., Fendt, S., 2020. Power-to-liquid via synthesis of methanol, DME or Fischer–Tropsch-fuels: a review. Energy Environ. Sci. 13, 3207–3252. https://doi.org/10.1039/D0EE01187H.

Barbosa-Cánovas, G.V., Ortega-Rivas, E., Juliano, P., Yan, H., 2005. Particle Properties. Food Engineering Series 19–54. https://doi.org/10.1007/0-387-27613-0_2.

Zhang, H., Xu, C., Yu, H., Wu, H., Jin, F., Xiao, F., et al., 2022. Enhancement of methanol steam reforming in a tubular fixed-bed reactor with simultaneous heating inside and outside. Energy 254, 124330. https://doi.org/10.1016/J.ENERGY.2022.124330.

Xuan, G., Mirko, E., Rodrigues, S.J., Vorhauer-Huget, N., Christian, L., Fond, B., 2024. Multi-point temperature measurements in packed beds using phosphor thermometry and ray tracing simulations. Particuology 85, 77–88. https://doi.org/10.1016/J.PARTIC.2023.03.015.

Schäfer T, Schubert M, Hampel U. Temperature Grid Sensor for the Measurement of Spatial Temperature Distributions at Object Surfaces. Sensors 2013, Vol 13, Pages 1593-1602 2013;13:1593–602. https://doi.org/10.3390/S130201593.

Bahiraei L. Improving the temperature measurement in hydro-processing reactors 2019.

Blay, V., Bobadilla, L.F., 2018. Numerical study of the accuracy of temperature measurement by thermocouples in small-scale reactors. Chem. Eng. Res. Des. 131, 545–556. https://doi.org/10.1016/J.CHERD.2017.06.003.

Kutscherauer, M., Reinold, P., Böcklein, S., Mestl, G., Turek, T., Wehinger, G.D., 2022. How Temperature Measurement Impacts pressure drop and Heat Transport in Slender Fixed Beds of Raschig Rings. ACS Eng. Au 3, 45–58. https://doi.org/10.1021/ACSENGINEERINGAU.2C00039.

Leonzio, G., Foscolo, P.U., 2020. Analysis of a 2-D model of a packed bed reactor for methanol production by means of CO2 hydrogenation. Int. J. Hydrogen Energy 45, 10648–10663. https://doi.org/10.1016/J.IJHYDENE.2020.01.248.

Rahimpour, M.R., Parvasi, P., Setoodeh, P., 2009. Dynamic optimization of a novel radial-flow, spherical-bed methanol synthesis reactor in the presence of catalyst deactivation using Differential Evolution (DE) algorithm. Int. J. Hydrogen Energy 34, 6221–6230. https://doi.org/10.1016/J.IJHYDENE.2009.05.068.

Parvasi, P., Rahimpour, M.R., Jahanmiri, A., 2008. Incorporation of Dynamic Flexibility in the Design of a Methanol Synthesis Loop in the Presence of Catalyst Deactivation. Chem. Eng. Technol. 31, 116–132. https://doi.org/10.1002/CEAT.200700209.

Zhu J, Araya SS, Cui X, Sahlin SL, Kær SK. Modeling and Design of a Multi-Tubular Packed-Bed Reactor for Methanol Steam Reforming over a Cu/ZnO/Al2O3 Catalyst.

Energies 2020, Vol 13, Page 610 2020;13:610. https://doi.org/10.3390/EN13030610.
Hafeez, S., Aristodemou, E., Manos, G., Al-Salem, S.M., Constantinou, A., 2020. Modelling of packed bed and coated wall microreactors for methanol steam reforming for hydrogen production. RSC Adv. 10, 41680–41692. https://doi.org/10.1039/D0RA06834A.
Bakhtiary H, Hayer F, Venvik H, Holmen A. Kinetics and Reactor Modeling of Methanol Synthesis from Synthesis Gas n.d. https://www.comsol.com/paper/kinetics-and-reactor-modeling-of-methanol-synthesis-from-synthesis-gas-5655 (accessed July 7, 2024).
Adji, B.S., Muharam, Y., Kartohardjono, S., 2019. Simulation of Methanol Synthesis from CO2 Hydrogenation in a Packed Bed Reactor using COMSOL Multiphysics. International Journal of Engineering Research and Technology 12, 2592–2599.
Rahimpour, M.R., 2008. A two-stage catalyst bed concept for conversion of carbon dioxide into methanol. Fuel Process. Technol. 89, 556–566. https://doi.org/10.1016/J.FUPROC.2007.10.011.
Zabiri H, Yusup S, Phuong Anh N. A simulation study of an industrial methanol reactor based on simplified steady-state model 2010.
Sadeghi, S., Vafajoo, L., Kazemeini, M., Fattahi, M., 2014. Modeling of the Methanol Synthesis Catalyst Deactivation in a Spherical Bed Reactor: an Environmental Challenge. APCBEE Proc. 10, 84–90. https://doi.org/10.1016/J.APCBEE.2014.10.021.
Maksimov, P., Laari, A., Ruuskanen, V., Koiranen, T., Ahola, J., 2021. Methanol synthesis through sorption enhanced carbon dioxide hydrogenation. Chem. Eng. J. 418, 129290. https://doi.org/10.1016/J.CEJ.2021.129290.
Shahrokhi, M., Baghmisheh, G.R., 2005. Modeling, simulation and control of a methanol synthesis fixed-bed reactor. Chem. Eng. Sci. 60, 4275–4286. https://doi.org/10.1016/J.CES.2004.12.051.
Masoudi, S., Farsi, M., Rahimpour, M.R., 2019. Dynamic optimization of methanol synthesis section in the dual type configuration to increase methanol production. Oil & Gas Science and Technology - Revue d'IFP Energies Nouvelles 74, 90. https://doi.org/10.2516/OGST/2019062.
Wang, X., Yue, H., Liu, G., Zhao, Z., 2011. The Application of COMSOL Multiphysics in Direct Current Method Forward Modeling. Procedia Earth Planet. Sci. 3, 266–272. https://doi.org/10.1016/J.PROEPS.2011.09.093.
Solsvik, J., Haug-Warberg, T., Jakobsen, H.A., 2016. Implementation of chemical reaction equilibrium by Gibbs and Helmholtz energies in tubular reactor models: Application to the steam–methane reforming process. Chem. Eng. Sci. 140, 261–278. https://doi.org/10.1016/J.CES.2015.10.011.
Gallucci, F., Paturzo, L., Basile, A., 2004. An experimental study of CO2 hydrogenation into methanol involving a zeolite membrane reactor. Chem. Eng. Process. 43, 1029–1036. https://doi.org/10.1016/J.CEP.2003.10.005.
Izbassarov, D., Nyári, J., Tekgül, B., Laurila, E., Kallio, T., Santasalo-Aarnio, A., et al., 2021. A numerical performance study of a fixed-bed reactor for methanol synthesis by CO2 hydrogenation. Int. J. Hydrogen Energy 46, 15635–15648. https://doi.org/10.1016/J.IJHYDENE.2021.02.031.
Lombardelli, G., Mureddu, M., Lai, S., Ferrara, F., Pettinau, A., Atzori, L., et al., 2022. CO2 hydrogenation to methanol with an innovative Cu/Zn/Al/Zr catalyst: Experimental tests and process modeling. J. CO2 Util. 65, 102240. https://doi.org/10.1016/J.JCOU.2022.102240.
Etim, U.J., Song, Y., Zhong, Z., 2020. Improving the Cu/ZnO-Based Catalysts for Carbon Dioxide Hydrogenation to Methanol, and the use of Methanol As a Renewable Energy Storage Media. Front Earth Sci (lausanne) 8, 545431. https://doi.org/10.3389/FENRG.2020.545431/BIBTEX.
Sahibzada, M., Metcalfe, I.S., Chadwick, D., 1998. Methanol Synthesis from CO/CO2/H2over Cu/ZnO/Al2O3at Differential and Finite Conversions. J. Catal. 174, 111–118. https://doi.org/10.1006/JCAT.1998.1964.
Vanden, B.KM., Froment, G.F., 1996. A Steady-State Kinetic Model for Methanol Synthesis and the Water Gas Shift Reaction on a Commercial Cu/ZnO/Al 2 O 3 Catalyst. J. Catal. 161, 1–10.
Villa, P., Forzattl, P., Buzzl-Ferrarls, G., Garone, G., Pasquon, I., 1985. Synthesis of Alcohols from Carbon Oxides and Hydrogen. 1. Kinetics of the Low-pressure Methanol Synthesis. Ind. Eng. Chem. Process. Des. Dev. 24, 12–19. https://doi.org/10.1021/I200028A003/ASSET/I200028A003.FP.PNG_V03.
Park, N., Park, M.J., Lee, Y.J., Ha, K.S., Jun, K.W., 2014. Kinetic modeling of methanol synthesis over commercial catalysts based on three-site adsorption. Fuel Process. Technol. 125, 139–147. https://doi.org/10.1016/J.FUPROC.2014.03.041.
Seidel, C., Jörke, A., Vollbrecht, B., Seidel-Morgenstern, A., Kienle, A., 2018. Kinetic modeling of methanol synthesis from renewable resources. Chem. Eng. Sci. 175, 130–138. https://doi.org/10.1016/J.CES.2017.09.043.
Peter, M., Fichtl, M.B., Ruland, H., Kaluza, S., Muhler, M., Hinrichsen, O., 2012. Detailed kinetic modeling of methanol synthesis over a ternary copper catalyst. Chem. Eng. J. 203, 480–491. https://doi.org/10.1016/J.CEJ.2012.06.066.
Kobl, K., Thomas, S., Zimmermann, Y., Parkhomenko, K., Roger, A.C., 2016. Power-law kinetics of methanol synthesis from carbon dioxide and hydrogen on copper–zinc oxide catalysts with alumina or zirconia supports. Catal. Today 270, 31–42. https://doi.org/10.1016/J.CATTOD.2015.11.020.
Slotboom, Y., Bos, M.J., Pieper, J., Vrieswijk, V., Likozar, B., Kersten, S.R.A., et al., 2020. Critical assessment of steady-state kinetic models for the synthesis of methanol over an industrial Cu/ZnO/Al2O3 catalyst. Chem. Eng. J. 389, 124181. https://doi.org/10.1016/J.CEJ.2020.124181.
Nyári, J., Izbassarov, D., Toldy, Á.I., Vuorinen, V., Santasalo-Aarnio, A., 2022. Choice of the kinetic model significantly affects the outcome of techno-economic assessments of CO2-based methanol synthesis. Energy Convers Manag 271, 116200. https://doi.org/10.1016/J.ENCONMAN.2022.116200.
Khawaja, S., Usman, M.R., 2024. Kinetics of CO2 hydrogenation to methanol over CuO/ZnO/ZrO2 catalyst: Comparison of the differential and integral methods of kinetic analysis. Int. J. Chem. Kinet. 56, 469–481. https://doi.org/10.1002/KIN.21720.
Portha, J.F., Parkhomenko, K., Kobl, K., Roger, A.C., Arab, S., Commenge, J.M., et al., 2017. Kinetics of Methanol Synthesis from Carbon Dioxide Hydrogenation over Copper-Zinc Oxide Catalysts. Ind. Eng. Chem. Res. 56, 13133–13145. https://doi.org/10.1021/ACS.IECR.7B01323.
Leonzio G. Methanol Synthesis: Optimal Solution for a Better Efficiency of the Process. Processes 2018, Vol 6, Page 20 2018;6:20. https://doi.org/10.3390/PR6030020.
Keil, F.J., 1999. Methanol-to-hydrocarbons: process technology. Microporous Mesoporous Mater. 29, 49–66. https://doi.org/10.1016/S1387-1811(98)00320-5.
Løvik I. Modelling, estimation and optimization of the methanol synthesis with catalyst deactivation. 126 s 2001.
Woods, A.W., 2014. Dispersion in porous media. Flow in Porous Rocks 70–91. https://doi.org/10.1017/CBO9781107588677.006.
COMSOL Multiphysics. Dispersion 2024. https://doc.comsol.com/5.6/doc/com.comsol.help.battery/battery_ug_chemsptrans.09.140.html (accessed July 7, 2024).
Enviro Wiki. Advection-Dispersion-Reaction Equation for Solute Transport - Enviro Wiki 2020. https://www.enviro.wiki/index.php?title=Advection-Dispersion-Reaction_Equation_for_Solute_Transport (accessed July 7, 2024).
Eslamloueyan, R., Khademi, M.H., 2010. A neural network-based method for estimation of binary gas diffusivity. Chemom. Intel. Lab. Syst. 104, 195–204. https://doi.org/10.1016/J.CHEMOLAB.2010.08.009.
Melzi N, Khaouane L, Ammi Y, Hanini S, Laidi M, Zentou H. Comparative Study of Predicting the Molecular Diffusion Coefficient for Polar and Non-polar Binary Gas Using Neural Networks and Multiple Linear Regressions n.d. https://doi.org/10.15255/KUI.2019.010.
Bannach N. Modeling Darcian and Non-Darcian Flow in Porous Media | COMSOL Blog 2020. https://www.comsol.com/blogs/modeling-darcian-and-non-darcian-flow-in-porous-media (accessed July 7, 2024).
Xu, P., Yu, B., 2008. Developing a new form of permeability and Kozeny–Carman constant for homogeneous porous media by means of fractal geometry. Adv. Water Resour. 31, 74–81. https://doi.org/10.1016/J.ADVWATRES.2007.06.003.
Elsanoose A, Abobaker E, Khan F, Rahman MA, Aborig A, Butt SD. Characterization of a Non-Darcy Flow and Development of New Correlation of NON-Darcy Coefficient. Energies 2022, Vol 15, Page 7616 2022;15:7616. https://doi.org/10.3390/EN15207616.
Geb, D., Zhou, F., Catton, I., 2012. Internal heat transfer coefficient determination in a packed bed from the transient response due to solid phase induction heating. J. Heat Transfer 134. https://doi.org/10.1115/1.4005098/455599.
Bavière, R., Favre-Marinet, M., Le Person, S., 2006. Bias effects on heat transfer measurements in microchannel flows. Int. J. Heat Mass Transf. 49, 3325–3337. https://doi.org/10.1016/J.IJHEATMASSTRANSFER.2006.03.014.
Bozorgan, N., Krishnakumar, K., Bozorgan, N., 2012. Numerical Study on Application of CuO-Water Nanofluid in Automotive Diesel Engine Radiator. Modern Mechanical Engineering 2012, 130–136. https://doi.org/10.4236/MME.2012.24017.
Zarghoon, S., Emebu, S., Matušů, R., Belavý, C., Bartalský, L., Ďuriš, S., et al., 2024. Full-state feedback LQR with integral gain for control of induction heating of steel billet. Engineering Science and Technology, an International Journal 55, 101721. https://doi.org/10.1016/J.JESTCH.2024.101721.
Pérez-Fortes, M., Schöneberger, J.C., Boulamanti, A., Tzimas, E., 2016. Methanol synthesis using captured CO2 as raw material: Techno-economic and environmental assessment. Appl. Energy 161, 718–732. https://doi.org/10.1016/J.APENERGY.2015.07.067.
Takagawa, M., Ohsugi, M., 1987. Study on reaction rates for methanol synthesis from carbon monoxide, carbon dioxide, and hydrogen. J. Catal. 107, 161–172. https://doi.org/10.1016/0021-9517(87)90281-8.
Gao, F., McClure, S.M., Cai, Y., Gath, K.K., Wang, Y., Chen, M.S., et al., 2009. CO oxidation trends on Pt-group metals from ultrahigh vacuum to near atmospheric pressures: a combined in situ PM-IRAS and reaction kinetics study. Surf. Sci. 603, 65–70. https://doi.org/10.1016/J.SUSC.2008.10.031.
Bampaou, M., Kyriakides, A.S., Panopoulos, K., Seferlis, P., Voutetakis, S., 2021. Modelling of Methanol Synthesis: improving Hydrogen Utilisation. Chem. Eng. Trans. 88, 931–936. https://doi.org/10.3303/CET2188155.
Xing, S., Zhao, C., Ban, S., Liu, Y., Wang, H., 2020. Thermodynamic performance analysis of the influence of multi-factor coupling on the methanol steam reforming reaction. Int. J. Hydrogen Energy 45, 7015–7024. https://doi.org/10.1016/J.IJHYDENE.2019.12.192.
Collins-Martinez, V., Escobedo Bretado, M., Meléndez Zaragoza, M., Salinas Gutiérrez, J., Ortiz, A.L., 2013. Absorption enhanced reforming of light alcohols (methanol and ethanol) for the production of hydrogen: Thermodynamic modeling. Int. J. Hydrogen Energy 38, 12539–12553. https://doi.org/10.1016/J.IJHYDENE.2012.11.146.
Leonzio, G., Zondervan, E., Foscolo, P.U., 2019. Methanol production by CO2 hydrogenation: Analysis and simulation of reactor performance. Int. J. Hydrogen Energy 44, 7915–7933. https://doi.org/10.1016/J.IJHYDENE.2019.02.056.

Liu, Q., Rogut, J., Chen, B., Falconer, J.L., Noble, R.D., 1996. Improved methanol yield from methane oxidation in a non-isothermal reactor. Fuel 75, 1748–1754. https://doi.org/10.1016/S0016-2361(96)00112-3.

Iyer, S.S., Renganathan, T., Pushpavanam, S., Vasudeva Kumar, M., Kaisare, N., 2015. Generalized thermodynamic analysis of methanol synthesis: effect of feed composition. J. CO2 Util. 10, 95–104. https://doi.org/10.1016/J.JCOU.2015.01.006.

Jahanmiri, A., Eslamloueyan, R., 2002. Optimal temperature profile in methanol synthesis reactor. Chem. Eng. Commun. 189, 713–741. https://doi.org/10.1080/00986440212475.

Rashid M. Automated lab-reactor experimenting in CO2 hydrogenation. LUT University, 2023.